

# JGR Atmospheres

## RESEARCH ARTICLE

10.1029/2022JD037924

### Key Points:

- Typhoon In-Fa plays a more critical role in the rainfall amplification than the western Pacific subtropical high
- The western Pacific subtropical high and Typhoon In-Fa majorly control the meridional and zonal moisture transports, respectively
- Diabatic heating plays a primary role in vertical motion during this heavy rainfall event

### Correspondence to:

G. Chen,  
cgh@mail.iap.ac.cn

### Citation:

Rao, C., Chen, G., & Ran, L. (2023). Effects of Typhoon In-Fa (2021) and the western Pacific subtropical high on an extreme heavy rainfall event in central China. *Journal of Geophysical Research: Atmospheres*, 128, e2022JD037924. <https://doi.org/10.1029/2022JD037924>

Received 26 SEP 2022

Accepted 14 MAR 2023

## Effects of Typhoon In-Fa (2021) and the Western Pacific Subtropical High on an Extreme Heavy Rainfall Event in Central China

Chenhong Rao<sup>1,2</sup> , Guanghua Chen<sup>1,2</sup> , and LingKun Ran<sup>1,2</sup>

<sup>1</sup>Key Laboratory of Cloud-Precipitation Physics and Severe Storms, Institute of Atmospheric Physics, Chinese Academy of Sciences, Beijing, China, <sup>2</sup>University of Chinese Academy of Sciences, Beijing, China

**Abstract** An extreme heavy rainfall event in Henan Province (HnHRE) of central China in July 2021, which is jointly affected by the western Pacific subtropical high (WPSH) and Typhoon In-Fa (2021), is comprehensively studied through five experiments conducted using the Weather Research and Forecasting Model (WRF). The patterns of the WPSH, In-Fa, and precipitation are well reproduced in the control experiment. The magnitude of potential vorticity (PV) anomaly associated with the WPSH (In-Fa) is increased and decreased by 50% in the initial condition based on the piecewise PV inversion method, namely, SH150 and SH050 (TC150 and TC050), respectively. The analysis shows that the 54-hr rainfall accumulations in TC150 and TC050 are reduced by 39.5% and 31.8%, respectively, more than 28.8% in SH150 and 20.1% in SH050, indicating that Typhoon In-Fa plays a more critical role in the rainfall amplification than the WPSH. This result also confirms that the HnHRE occurs within the quite favorable configuration of WPSH and In-Fa circulations. The WPSH and In-Fa majorly control the meridional and zonal moisture transports, respectively. The diagnosis of moist ageostrophic  $\omega$  turns out that diabatic heating is closely related to the vertical motion during the HnHRE. Besides, the heavy rainfall region is also closely attributed to the distributions of equivalent potential temperature and divergence.

**Plain Language Summary** This study focuses on a typical heavy rainfall event (HRE) related to the western Pacific subtropical high (WPSH) and Typhoon In-Fa (2021). The study aims to quantitatively analyze the effects of the WPSH and In-Fa and their interactions, which play a vital role in the HRE. The distribution and amount of rainfall are reasonably reproduced in a numerical model. Moreover, the four sensitivity experiments are conducted to identify the influence of the WPSH and In-Fa on the HRE. The results confirm that the HRE occurs under the highly favorable WPSH and In-Fa circulations and their cooperation. Typhoon In-Fa plays a more critical role in rainfall amplification than the WPSH. This finding emphasizes that the interaction of the WPSH and typhoon has an important effect on the HRE.

## 1. Introduction

Heavy rainfall events (HREs) have great socioeconomic impacts around the world and cause deadly and destructive disasters. China is located in the East Asia monsoon area and frequently susceptible to heavy rainfall and flooding extremes (Cao & Gao, 2007; H. Li et al., 2017). Studies on HREs have always been concerned widely and highly (Chen et al., 2012; Junker et al., 1999).

Although HREs generally have a short-lived and localized nature (Jo et al., 2020), they are actually modulated by synoptic-scale systems, such as the western Pacific subtropical high (WPSH, Ding & Chan, 2005), tropical cyclone (TC, also known as typhoon, Ross & Kurihara, 1995), and southeasterly moisture transport produced by their interaction (Y. Nie & Sun, 2022). H. Wang et al. (2021) divided the persistent HREs over the Yangtze-Huaihe River Valley during 1981–2020 into three types according to pattern correlation. They emphasized that the WPSH and TC play significant roles in persistent HREs. Y. Wang et al. (2009) performed numerical sensitivity experiments to suggest that Typhoon Songda (2004) enhanced the transport of moisture to the heavy rainfall region through the outer circulation and was responsible for >90% of the precipitation in Japan. Many studies have revealed that when a TC approaches the WPSH, the pressure gradient between them increases rapidly, establishing or strengthening the low-level easterly jet, which is beneficial to transport water vapor toward the heavy rainfall region (Schumacher et al., 2011).

Sufficient moisture is one of the necessary conditions for HREs. A number of studies quantitatively calculate the moisture content in the rainfall region. Y. Zhang et al. (2019) calculated the moisture flux through the four boundaries of the Sichuan Basin, and the net moisture flux into this region, showing that the southeastern (southwestern, northeastern, and northwestern) boundary was a major channel for water vapor transport into (out of) the basin. The result from Xia et al. (2021) also supported this conclusion. Zhao et al. (2020) indicated that the moisture in North China was mainly imported from the western and southern sides, and the moisture supply from the south side played a more critical role. In addition, the major contribution of moisture flux convergence is due to the convergence of horizontal wind rather than moisture advection, implying that the precipitation is more directly related to vertical motion than horizontal transport.

Heavy rainfall is accompanied by strong vertical motion, which can lift water vapor, momentum, and heat energy from the lower level to the upper level, and thus generate the release of diabatic heating and the conversion of potential energy to kinetic energy. Generally, the atmosphere vertical velocity is hardly measured directly and usually derived by diagnostic method via other physical quantities, such as Q-vector (Yao et al., 2004; Yue et al., 2003, 2015), helicity (Bogner et al., 2000; Kain et al., 2008), and potential vorticity (Hoskins et al., 1978; X. Wang & Zhang, 2003; D. Zhang & Kieu, 2006). It is worth noting that, by comparison with other methods, the *Q*-vector is known as the best tool for calculating vertical velocity (Dunn, 1991).

Hoskins et al. (1978) introduced quasi-geostrophic *Q*-vector, acting as a unique forcing term in the  $\omega$  (vertical velocity in a *p*-coordinate system) equation which can be handily calculated using single-level observational data. Since then, the *Q*-vector has been utilized extensively in various forms, including generalized *Q*-vector (Davies-Jones, 1991), *C*-vector (Xu, 1992), and ageostrophic *Q*-vector (X. Zhang, 1999). The various *Q*-vector forms of  $\omega$  equation have been widely applied to study TCs (Viúdez et al., 1996), Mei-Yu fronts (Gu et al., 2018), and HREs (Martius et al., 2008). However, most of the previous *Q*-vector analyses only consider the influence of dynamic forcings on vertical motion, which are associated with the adiabatically balanced flow. In fact, a large amount of heating is released during HREs due to water vapor condensation, and the diabatic heating can also drive strong vertical motion (Horinouchi & Hayashi, 2017; J. Nie & Sobel, 2016). Considering the impact of diabatic heating, X. Zhang (1999) derived a diagnostic equation of moist ageostrophic (MAG) *Q*-vector in a *z*-coordinate system, and then Yao and Yu (2000) deduced it based on the primitive equation sets in a *p*-coordinate system. These two expressions can be converted by coordinate transformation. In MAG *Q*-vector equation, vertical motion can be diagnosed by computing MAG *Q*-vector convergence. Many studies have indicated that the strong convergence of the MAG *Q*-vector is collocated with the heavy rainfall region, and the convergence intensity is well positively correlated with the precipitation intensity (Meng & Wang, 2016; Yao et al., 2004). Most of the previous studies employed diagnostic methods to analyze qualitatively the vertical velocity, but few quantitatively calculated the vertical movement by numerical inversion. One of attempts in this study is made to quantify the contribution of dynamic forcing and diabatic heating to  $\omega$  and compare their relative contribution to an extreme HRE.

An extreme HRE struck Henan Province in central China during 17–23 July 2021 (hereafter, HnHRE), characterized by a long duration, a record-breaking hourly rain rate, and heavy rainfall accumulation. The HnHRE caused nearly 400 people to be dead and missing and \$17.65 billion direct economic loss. Recent studies indicated that the HnHRE took place in an anomalous synoptic circulation pattern, namely, the coexistence of a northwestward-shifting WPSH, Typhoon In-Fa (2021) over the East China sea, and Typhoon Cempaka (2021) over the South China Sea (Deng et al., 2022; Fu et al., 2022; Y. Nie & Sun, 2022; Xu, Duan, & Xu, 2022, 2022b). Rao et al. (2022) conducted a series of numerical experiments, concluding that Typhoon In-Fa had a more significant impact on the HnHRE than Typhoon Cempaka. Since Typhoon In-Fa was located on the southern flank of the WPSH, the strong low-level easterly or southeasterly jet emerged between the WPSH and Typhoon In-Fa, which transported abundant moisture from ocean to Henan Province to fuel heavy rainfall. Therefore, it is intriguing to fully understand how the cooperation between the WPSH and In-Fa affects the HnHRE and what their individual contributions are, as well as what factors are responsible for the heavy rainfall region. To answer these questions, the piecewise potential vorticity inversion (PPVI) method (Davis & Emanuel, 1991) will be first applied to amplify and diminish the WPSH and Typhoon In-Fa separately, and then the accumulated precipitation, moisture transport, moist ageostrophic  $\omega$ , equivalent potential temperature ( $\theta_e$ ), and other dynamical factors will be thoroughly analyzed in a series of numerical experiments. Through these analyses, the mechanism underlying the effect of the WPSH and In-Fa on the HnHRE is revealed, which has not yet received much attention in previous studies.

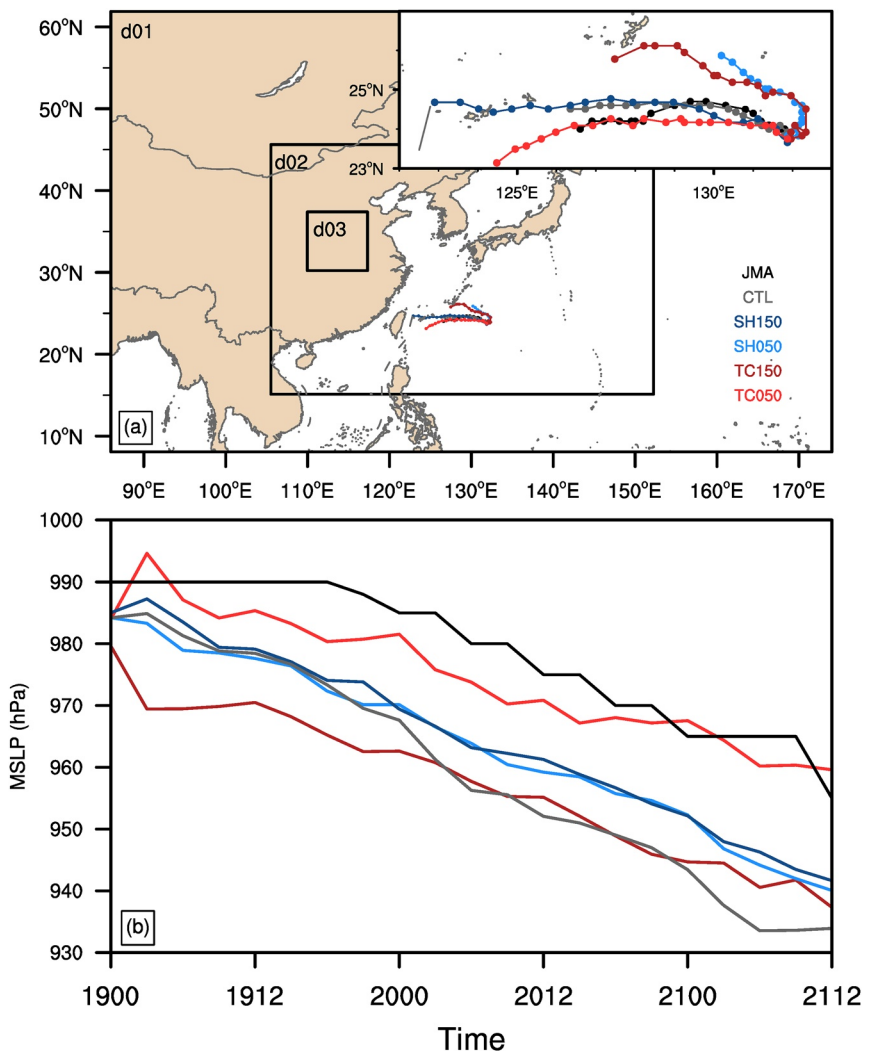


**Figure 1.** (a) Three domains of the Weather Research and Forecasting experiments, JMA best track (black) and simulated Typhoon In-Fa tracks (gray, dark blue, light blue, dark red, and light red represent CTL, SH150, SH050, TC150, and TC050, respectively) with 3-hr intervals from 0000 UTC 19 July to 1200 UTC 21 July. (b) Time series of the observed and simulated minimum sea level pressure (MSLP, units: hPa) of Typhoon In-Fa.

The remaining sections of this paper are organized as follows. Section 2 introduces the methodology and experiment design. The synoptic environmental pattern during the period of HnHRE is presented in Section 3. The impacts of the WPSH and Typhoon In-Fa on moisture transport and vertical velocity in the HnHRE region are elucidated in Section 4. The summary and discussion are given in Section 5.

## 2. Methodology and Experiment Design

### 2.1. Experiment Design

The Advanced Research version of the Weather Research and Forecasting Model (WRF-ARW), version 3.6.1 (Skamarock & Klemp, 2008), is used for numerical simulations in this study. Three two-way interactive domains are initialized with horizontal resolutions of 27, 9, and 3 km,  $316 \times 256$ ,  $502 \times 388$ , and  $238 \times 280$  grid points, respectively (Figure 1a). The model has 45 levels in vertical with higher vertical resolution in the boundary and near the tropopause, and the model top is set at 10 hPa. The initial and boundary conditions are derived from the 6-hourly National Centers for Environmental Prediction (NCEP) global final (FNL) analysis data set at  $1^\circ \times 1^\circ$  resolution. The Kain-Fritsch cumulus scheme (Kain & Fritsch, 1990) is only adopted in the outmost domain. The WSM6 microphysics scheme (Hong et al., 2004), Monin-Obukhov surface layer scheme (Monin

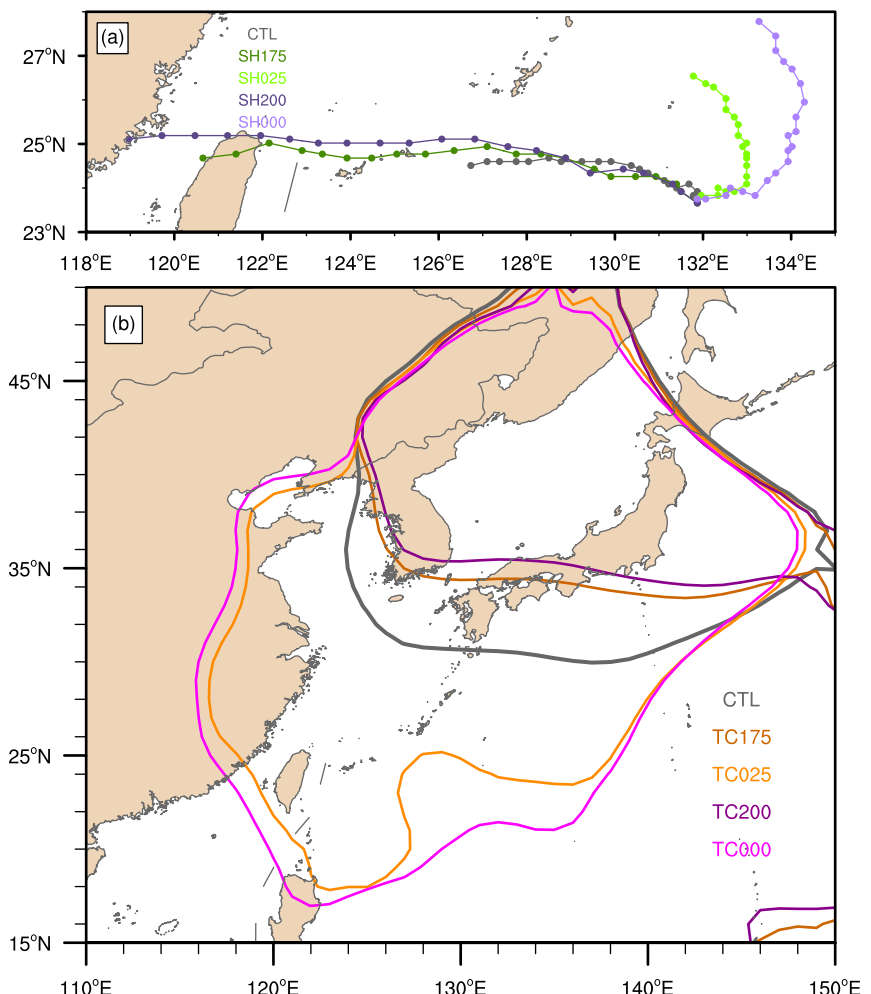


**Figure 2.** (a) The simulated In-Fa tracks (gray, dark green, light green, dark purple, and light purple in CTL, SH175, SH025, SH200, and SH000, respectively) with 3-hr intervals from 0000 UTC 19 July to 1200 UTC 21 July. (b) The 5880-gpm contour of the WPSH (gray, dark orange, light orange, dark magenta, and light magenta in CTL, TC175, TC025, TC200, and TC000, respectively) at 0000 UTC 20 July.

& Obukhov, 1954), and YSU planetary boundary scheme (Hong et al., 2009) are used. In addition, longwave radiation and shortwave radiation are parameterized with the Rapid Radiation Transfer Model (RRTM) scheme (Iacono et al., 2000) and the Dudhia scheme (Dudhia, 1989), respectively. All the domains are initialized at 0000 UTC 19 July and integrated for 60 hr.

Major five numerical experiments are performed to examine the impacts of the WPSH and Typhoon In-Fa during the HnHRE. In the control experiment (CTL), the WPSH and In-Fa are intact throughout the simulation period. The other four sensitivity experiments, in which the zonal and meridional wind components ( $U$  and  $V$ ), geopotential ( $\Phi$ ), and temperature ( $T$ ) of the WPSH (In-Fa) are increased and decreased by 50% in the initial condition by inverting its 150% and 50% PV anomalies using the PPVI method (details in Section 2.2), are designated as SH150 and SH050 (TC150 and TC050), respectively.

To test the sensitivity of the simulation to the WPSH and In-Fa structures and intensities, the supplementary experiments are also conducted with the circulation of an individual system strengthened or weakened by 25%, 75%, and 100% (denoted as SH125/175/200, TC125/175/200, SH075/025/000, TC075/025/000), respectively. In SH175/200 with a large enhancement of the WPSH, the Typhoon In-Fa moves much fast and passes over Taiwan due to the strong steering flows on the southern side of the WPSH (dark green and dark purple tracks in Figure 2a), which would bring qualitatively different impacts on the rainfall region. In SH025/000 with a large weakening of the WPSH, the simulated In-Fa is shifted northward or northeastward (light green

and light purple tracks in Figure 2a), quite different from the western track in CTL (gray track in Figure 2a). The TC circulation increased by 75% or 100% has little effect on the WPSH with a slight northward retreat (dark orange and dark magenta contours in Figure 2b), while the WPSH expands significantly with the area approximately twice as large as that in CTL at 0000 UTC 20 July if the TC circulation is decreased by 75% or 100% (light orange and light magenta contours in Figure 2b). Therefore, if one system is changed to a large degree due to the modification of the other system, it is difficult to distinguish the relative influence of individual systems on heavy rainfall. Besides, in the experiments with the increase and decrease by 25% in the circulations of the WPSH or In-Fa (i.e., SH125, SH075, TC125, TC075), the results are qualitatively similar to the conclusions in this study except that the structures and intensities related to precipitation and synoptic systems vary to a relatively lesser extent as opposed to the counterparts in the present sensitivity experiments (not shown). Hence, the following sections will only focus on the results in SH150, TC150, SH050, and TC050.

## 2.2. Piecewise Potential Vorticity Inversion

PV thinking is a useful tool to understand the evolution of synoptic system in the atmosphere (Hoskins et al., 1985). PV is defined based on absolute vorticity and static stability (potential temperature ( $\theta$ ) gradient), reflecting both the thermodynamic and dynamic state of the atmosphere. According to the PV invertibility principle, the balanced wind and mass fields can be inverted, given PV distribution and boundary conditions. The PPVI method was proposed and then widely applied (Davis, 1992; Davis & Emanuel, 1991; Wu et al., 2012; Wu & Emanuel, 1995a, 1995b; Wu et al., 2003; Yan et al., 2021). Using PPVI method, the total PV perturbation field can be obtained by subtracting a mean field from a total field, and then the individual perturbed PV patches corresponding to synoptic systems of concern can invert separately to obtain balanced wind and mass fields. In this study, the PPVI method is applied to isolate the circulations of the WPSH and In-Fa and assess their relative influences on the rainfall intensity and region during the HnHRE.

The PPVI method is based on the following equations (Davis & Emanuel, 1991):

$$\nabla^2\Phi = \nabla \cdot (f \nabla \Psi) + \frac{2}{a^4 \cos^2 \varphi} \frac{\partial(\partial\Psi/\partial\lambda, \partial\Psi/\partial\varphi)}{\partial(\lambda, \varphi)} \quad (1)$$

$$q = \frac{g\kappa\pi}{p} \left[ (f + \nabla^2\Psi) \frac{\partial^2\Phi}{\partial\pi^2} - \frac{1}{a^2 \cos^2 \varphi} \frac{\partial^2\Psi}{\partial\lambda\partial\pi} \frac{\partial^2\Phi}{\partial\lambda\partial\pi} - \frac{1}{a^2} \frac{\partial^2\Psi}{\partial\varphi\partial\pi} \frac{\partial^2\Phi}{\partial\varphi\partial\pi} \right] \quad (2)$$

where  $\Phi$  and  $\Psi$  represent geopotential and streamfunction, respectively;  $a$  for earth's radius;  $\lambda$  and  $\varphi$  for longitude and latitude, respectively.  $q$  stands for PV;  $g$  is the gravitational acceleration;  $\kappa = R_d/C_p$ , with  $R_d$  and  $C_p$  present the gas constant and the specific heat capacity, respectively;  $\pi$  [ $\pi = C_p(p/p_0)^\kappa$ ] is the Exner function, which defines a vertical coordinate;  $f$  for the Coriolis parameter. Given the distribution of PV, lateral boundary conditions of  $\Phi$  and  $\Psi$  on the upper and lower boundaries, the distribution of dynamically balanced  $\Phi$  and  $\Psi$  can be solved using the successive overrelaxation method (Davis & Emanuel, 1991). The nondivergent wind and  $\theta$  can be obtained by the following two relations:

$$\vec{V} = \mathbf{k} \times \nabla\Psi \text{ and } \theta = -\partial\Phi/\partial\pi \quad (3)$$

This study takes the time average for July 2010–2019 as the mean state (Davis & Emanuel, 1991; Wu & Emanuel, 1995a). The mean streamfunction field ( $\bar{\Psi}$ ) is derived from the time-averaged wind field. The associated mean geopotential field ( $\bar{\Phi}$ ) and mean PV field ( $\bar{q}$ ) can be derived using nonlinear balance equations (as in Equations 1 and 2, with the replacement  $\Psi, \Phi, q$  by  $\bar{\Psi}, \bar{\Phi}, \bar{q}$ ; Wu et al., 2003). The perturbation equations can be obtained by the total equations minus the mean. To relate the PV perturbation to the flow perturbation, the star variables are defined as  $(\cdot)^* = \bar{(\cdot)} + \frac{1}{2} \sum_{k=1}^K (\cdot)_k'$ , that is, the mean plus half the total perturbation. The balanced perturbation fields in response to each PV anomaly can be inverted by these equations (Davis, 1992; Davis & Emanuel, 1991):

$$\nabla^2\Phi'_k = \nabla \cdot (f \nabla \Psi'_k) + \frac{2}{a^4 \cos^2 \varphi} \left[ \frac{\partial^2\Psi^*}{\partial\lambda^2} \frac{\partial^2\Psi'_k}{\partial\varphi^2} + \frac{\partial^2\Psi^*}{\partial\varphi^2} \frac{\partial^2\Psi'_k}{\partial\lambda^2} - 2 \frac{\partial^2\Psi^*}{\partial\lambda\partial\varphi} \frac{\partial^2\Psi'_k}{\partial\lambda\partial\varphi} \right] \quad (4)$$

$$q'_k = \frac{g\kappa\pi}{p} \left[ \left( f + \nabla^2 \Psi^* \right) \frac{\partial^2 \Phi'_k}{\partial \pi^2} + \frac{\partial^2 \Phi^*}{\partial \pi^2} \nabla^2 \Psi'_k - \frac{1}{a^2 \cos^2 \varphi} \left( \frac{\partial^2 \Psi^*}{\partial \lambda \partial \pi} \frac{\partial^2 \Phi'_k}{\partial \lambda \partial \pi} + \frac{\partial^2 \Phi^*}{\partial \lambda \partial \pi} \frac{\partial^2 \Psi'_k}{\partial \lambda \partial \pi} \right) \right. \\ \left. - \frac{1}{a^2} \left( \frac{\partial^2 \Psi^*}{\partial \varphi \partial \pi} \frac{\partial^2 \Phi'_k}{\partial \varphi \partial \pi} + \frac{\partial^2 \Phi^*}{\partial \varphi \partial \pi} \frac{\partial^2 \Psi'_k}{\partial \varphi \partial \pi} \right) \right] \quad (5)$$

The sum of the individual perturbation fields  $q'_k$  is equal to the total perturbation field  $q'$ . Given the distribution of  $q'_k$ , and the boundary conditions of  $\Phi'_k$  and  $\Psi'_k$ , the distribution of  $\Phi'_k$  and  $\Psi'_k$  can be solved using the successive overrelaxation method. The flow perturbation fields associated with  $\Phi'_k$  and  $\Psi'_k$  are linearly superposable.

In SH150 and SH050, the whole PV anomaly is divided into two parts: one is the PV anomaly associated with WPSH ( $q'_{\text{WPSH}}$ ), the other is associated with the environmental  $q'$  outside the WPSH ( $q'_{\text{noWPSH}}$ ). Note that by definition,  $q' = q'_{\text{WPSH}} + q'_{\text{noWPSH}}$ . In order to better capture the region of WPSH,  $q'_{\text{WPSH}}$  is identified as a three-dimensional PV anomaly with less than  $-0.1$  PVU from 1,000 to 1200 hPa within the region surrounded by the contour of 5,880 gpm at 500 hPa. Likewise, TC150 and TC050 have the similar design as in SH150 and SH050, but for the PV anomaly associated with Typhoon In-Fa ( $q'_{\text{TY}}$ ).  $q'_{\text{TY}}$  is defined as a three-dimensional PV anomaly with greater than  $0.1$  PVU around In-Fa.

To examine how well the PPVI method performs in this study, the total flow fields obtained from the FNL data and inverted by the total PV at 0000 UTC 19 July are compared in Figures 3a and 3b. The total PV-inverted field (Figure 3b) can accurately reproduce the main characteristics of the WPSH and Typhoon In-Fa in terms of intensity, location, and size. In Figures 3c and 3d (Figures 3e and 3f), the circulation related to the WPSH (In-Fa) is increased and reduced by 50% relative to the total PV-inverted field (Figure 3b). Overall, the PPVI method yields reasonably the strengthened and weakened structure of the WPSH and In-Fa, which are designated as the initial conditions in the different sensitivity experiments.

### 2.3. Moist Ageostrophic $\omega$ Equation

The MAG  $\omega$  equation is a useful tool for understanding and quantifying the factors associated with vertical motion during the HREs. The  $Q$ -vector-form MAG  $\omega$  equation may be written as (Yao et al., 2004):

$$\left( \sigma_0 \nabla^2 + f_0^2 \frac{\partial^2}{\partial p^2} \right) \omega = -2 \nabla \cdot (\mathbf{Q}_{\text{Dia}}^* + \mathbf{Q}_{\text{Dyn}}^*) \quad (6)$$

where  $\nabla^2 = \partial^2 / \partial x^2 + \partial^2 / \partial y^2$ ,  $\nabla = (\partial / \partial x)\mathbf{i} + (\partial / \partial y)\mathbf{j}$ . The  $\mathbf{i}$  and  $\mathbf{j}$  are the unit vectors in the zonal and meridional directions, respectively. The static stability parameter,  $\sigma_0 = -(1/\rho_0)(d \ln \theta / dp)$ ,  $\rho_0 = 1.173 \text{ kg m}^{-3}$ . The Coriolis parameter  $f_0$  is defined at 35°N. On the right-hand side of Equation 6,  $Q$ -vector ( $\mathbf{Q}^*$ ) is divided into dynamic term ( $\mathbf{Q}_{\text{Dyn}}^*$ ) and diabatic term ( $\mathbf{Q}_{\text{Dia}}^*$ ), which can be expressed in the Cartesian coordinate as

$$\mathbf{Q}_{\text{Dia}}^* = Q_{\text{Dia},x}^* \mathbf{i} + Q_{\text{Dia},y}^* \mathbf{j} \text{ and } \mathbf{Q}_{\text{Dyn}}^* = Q_{\text{Dyn},x}^* \mathbf{i} + Q_{\text{Dyn},y}^* \mathbf{j} \quad (7)$$

where

$$Q_{\text{Dia},x}^* = \frac{1}{2} \left[ \frac{\partial(\gamma H)}{\partial x} \right] \text{ and } Q_{\text{Dyn},x}^* = \frac{1}{2} \left[ f_0 \left( \frac{\partial v}{\partial p} \frac{\partial u}{\partial x} - \frac{\partial u}{\partial p} \frac{\partial v}{\partial x} \right) - \gamma \frac{\partial \bar{V}}{\partial x} \cdot \nabla \theta \right] \quad (8a)$$

$$Q_{\text{Dia},y}^* = \frac{1}{2} \left[ \frac{\partial(\gamma H)}{\partial y} \right] \text{ and } Q_{\text{Dyn},y}^* = \frac{1}{2} \left[ f_0 \left( \frac{\partial v}{\partial p} \frac{\partial u}{\partial y} - \frac{\partial u}{\partial p} \frac{\partial v}{\partial y} \right) - \gamma \frac{\partial \bar{V}}{\partial y} \cdot \nabla \theta \right] \quad (8b)$$

$u$  and  $v$  represent the zonal and meridional wind components, respectively. The  $\gamma$  is  $(R_d/p)(p/p_0)^{\kappa}$ ,  $p_0 = 1,000 \text{ hPa}$ .  $H$  is the diabatic heating rate per unit mass, it is calculated in pressure coordinates using the thermodynamic equations (Ling & Zhang, 2012; Yanai et al., 1973):

$$H = \frac{\partial \theta}{\partial t} + \bar{V} \cdot \nabla \theta + \omega \frac{\partial \theta}{\partial p} \quad (9)$$

where  $\partial \theta / \partial t$  and  $\omega$  are output from the numerical model.

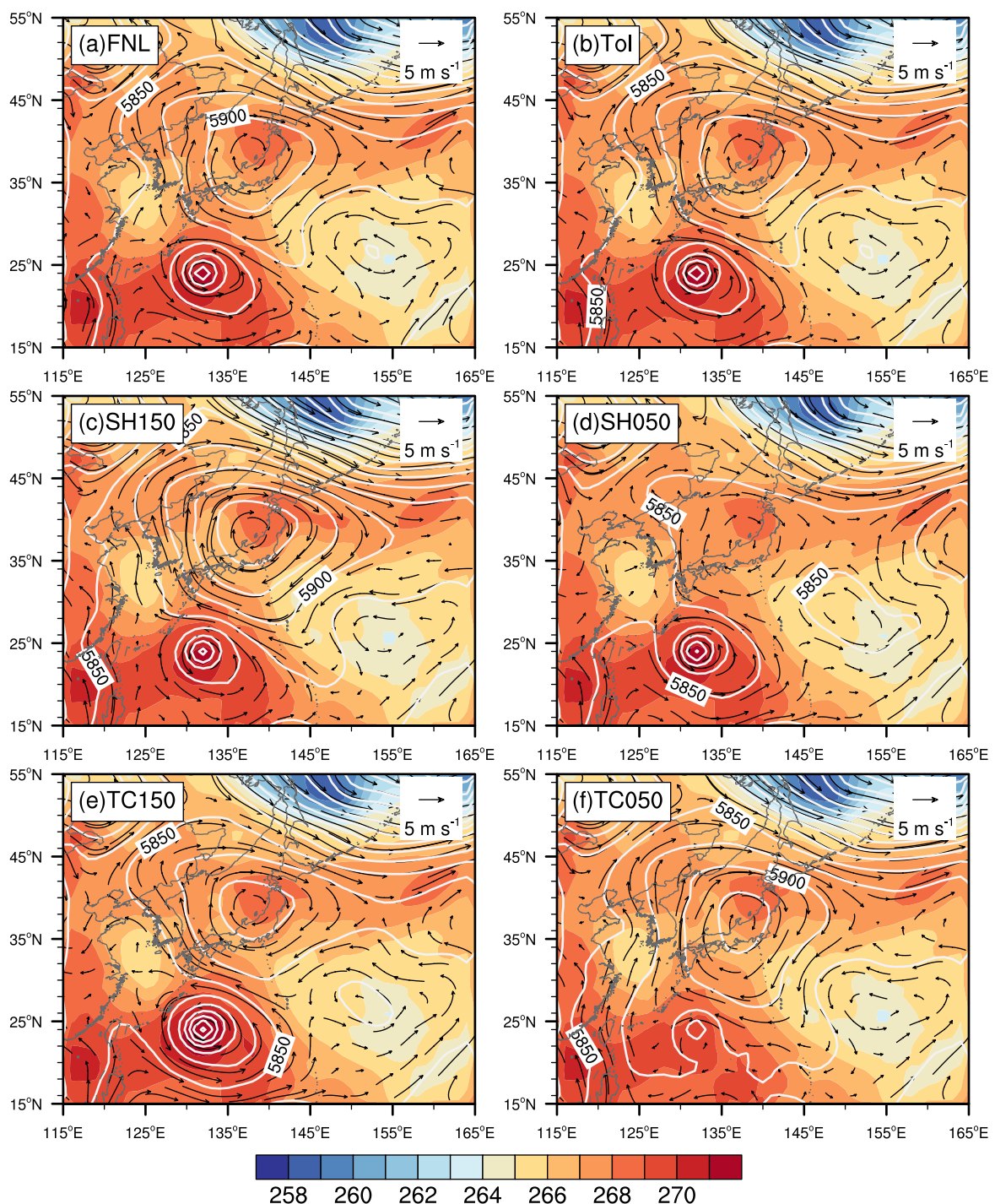


**Figure 3.** The 850-hPa temperature (shaded, units: K), horizontal wind (vectors, units: m s<sup>-1</sup>), and 500-hPa geopotential height (contours, units: gpm) (a) obtained from the final data, (b) inverted from the total potential vorticity, and in (c) SH150, (d) SH050, (e) TC150, and (f) TC050 using piecewise potential vorticity inversion method at the integration initial time of 0000 UTC 19 July.

Considering the two forcing terms on the right-hand side of Equation 6, the MAG  $\omega$  ( $\omega_{\text{MAG}}$ ) can be separated into two parts:  $\omega_{\text{Dia}}$  and  $\omega_{\text{Dyn}}$ , which are associated with the diabatic forcing and dynamic forcing, respectively. Therefore, we obtain

$$\omega_{\text{MAG}} = L^{-1}[-2\nabla \cdot (\mathbf{Q}_{\text{Dia}}^* + \mathbf{Q}_{\text{Dyn}}^*)] \quad (10a)$$

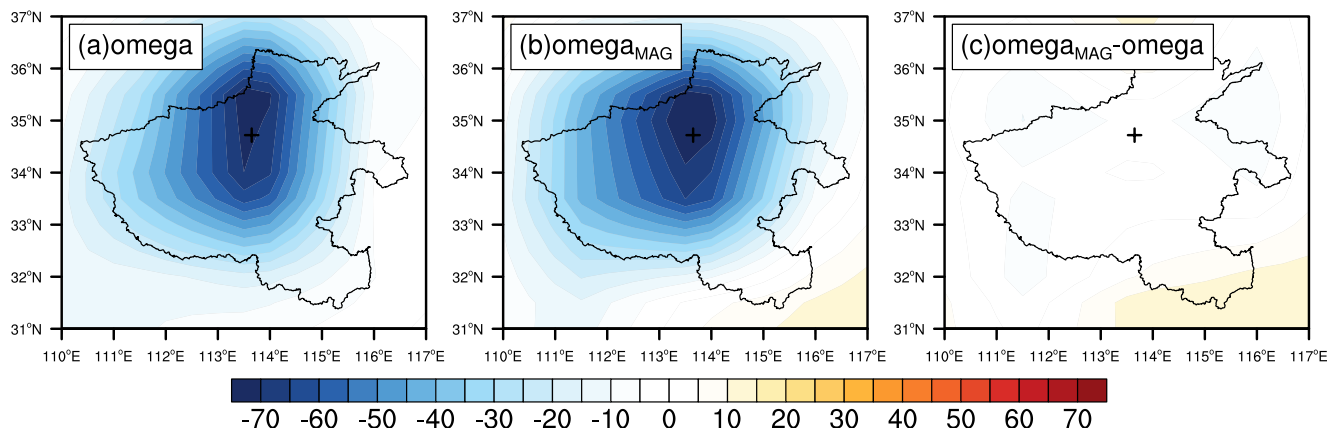


**Figure 4.** (a)  $\omega$ , (b)  $\omega_{\text{MAG}}$ , and (c) the difference between (a and b) at 500 hPa (shaded, units:  $\text{Pa s}^{-1}$ ) averaged from 0600 UTC 19 July to 1200 UTC 21 July. The black line represents the boundary of Henan Province and the plus sign represents Zhengzhou station.

$$\omega_{\text{Dia}} = L^{-1}(-2\nabla \cdot \mathbf{Q}_{\text{Dia}}^*) \text{ and } \omega_{\text{Dyn}} = L^{-1}(-2\nabla \cdot \mathbf{Q}_{\text{Dyn}}^*) \quad (10b)$$

where  $L$  is the linear differential operator formulated as  $L = \sigma_0 \nabla^2 + f_0^2 \frac{\partial^2}{\partial p^2}$ . Note that  $\omega_{\text{MAG}} = \omega_{\text{Dia}} + \omega_{\text{Dyn}}$ . The vertical velocity of the HnHRE is iteratively solved by the successive overrelaxation method (Zhao et al., 2022). The lower and upper boundary conditions set  $\omega_{\text{MAG}}$  to be zero at 1,000 and 200 hPa.

Figure 4 presents the comparison of simulated 500-hPa  $\omega$  (from the WRF) and diagnosed  $\omega_{\text{MAG}}$  in Henan Province averaged from 0600 UTC 19 July to 1200 UTC 21 July. It is obvious that  $\omega_{\text{MAG}}$  is quite coincident with  $\omega$ , in terms of magnitude and spatial distribution (Figures 4a and 4b) with a negligible positive difference in the southeast of Henan Province (Figure 4c), suggesting that the simulated  $\omega$  can be well reproduced by the diagnosed  $\omega_{\text{MAG}}$ .

#### 2.4. Moisture Transport

The vertical integrated moisture transport (IMT) averaged over the side  $i$  (where  $i$  refers to E (East), W (West), S (South), N (North)) of the target region is expressed as follows (Y. Nie & Sun, 2022; Xia et al., 2021; S. Zhang et al., 2022):

$$\text{IMT}_i = -\frac{1}{g \cdot S_i} \int_0^{S_i} \int_{1,000}^{p_t} (sh \cdot v_n) dp ds \quad (11)$$

where  $S_i$  is the length of side  $i$ ,  $p_t$  stands for top-level pressure;  $sh$  represents specific humidity; and  $v_n$  is wind component normal to the side, which is positive inward and negative outward. The net IMT refers to the sum of the  $\text{IMT}_i$  on the four sides of the target region. In this case, most of the atmospheric moisture resides below 400 hPa, herein the top-level pressure  $p_t$  is set 400 hPa.

### 3. Synoptic Environment

#### 3.1. Rainfall Characteristics

The HnHRE occurred during 17–23 July 2021, with the maximum accumulated precipitation of 1,122.6 mm. During this period, the maximum hourly rainfall at Zhengzhou station reached 201.9 mm, breaking the historical record of hourly precipitation in mainland China. The rain during the 7-day period was not evenly spatiotemporally distributed with the torrential rainfall mainly occurring from 0000 UTC 19 to 1200 UTC 21 July, which was selected for simulation. The precipitation process can be divided into three periods: During the first day (Figure 5a, beginning from 0000 UTC 19 July), the heavy rainfall was mainly distributed to the southwest of Zhengzhou station; The second day was the most intense period of the HnHRE with the heavy rainfall centered around Zhengzhou station (Figure 5b); After 0000 UTC 21 July (Figure 5c), the center of heavy rainfall moved to the northern part of Henan Province, and the precipitation intensity became weakened.

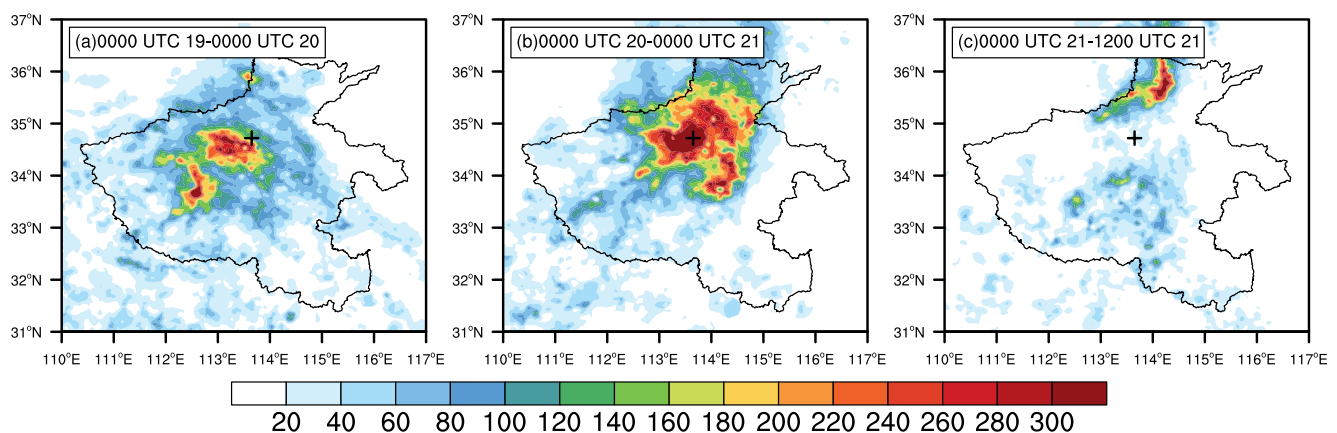


**Figure 5.** The spatial distributions of the accumulated rainfall in the observations during (a) 0000 UTC 19 July-0000 UTC 20 July, (b) 0000 UTC 20 July-0000 UTC 21 July, and (c) 0000 UTC 21 July-1200 UTC 21 July (shaded, units: mm). The black line represents the boundary of Henan Province and the plus sign represents Zhengzhou station.

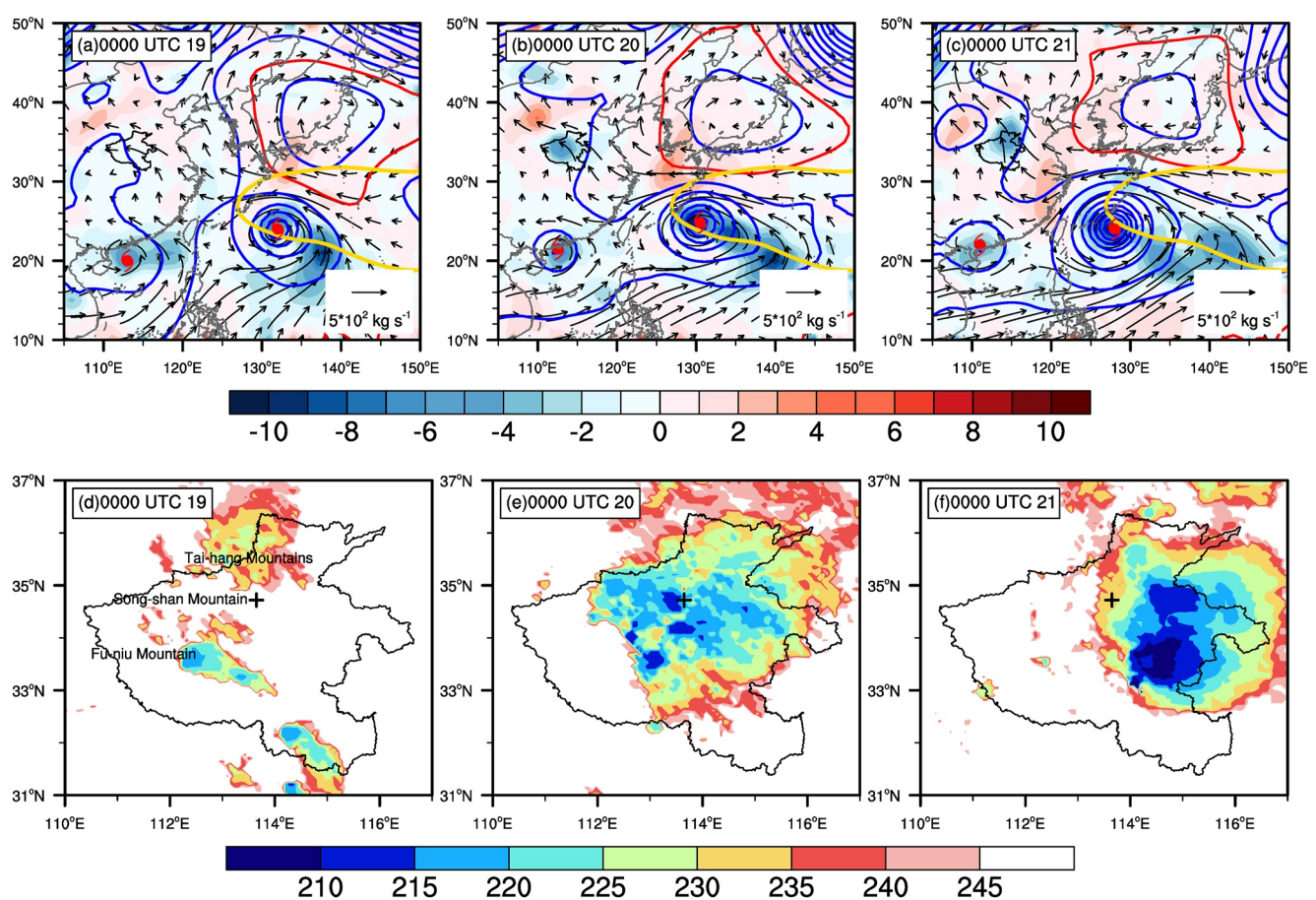


**Figure 6.** The integrated moisture transport (IMT) (vectors, units:  $5 \times 10^2 \text{ kg s}^{-1}$ ), IMT convergence (shaded, units:  $10^{-5} \text{ kg m}^{-2} \text{ s}^{-1}$ ), and 500-hPa geopotential height (blue contours start from 5,720 gpm with intervals of 20 gpm, contour of 5,880 gpm is red, and the yellow contour stands for 5,880 gpm averaged for 2010–2019) from the FNL data at (a) 0000 UTC 19 July, (b) 0000 UTC 20 July, and (c) 0000 UTC 21 July. The TBB (shaded, units: K) from the GridSat-B1 IR brightness temperature data at (d) 0000 UTC 19 July, (e) 0000 UTC 20 July, and (f) 0000 UTC 21 July. The black line represents the boundary of Henan Province and the plus sign represents Zhengzhou station.

### 3.2. Synoptic Pattern

Figures 6a–6c display a weather chart based on the FNL data from 0000 UTC 19 July to 0000 UTC 21 July with an interval of 24 hr. Figures 6d–6f show the evolution of the mesoscale convective system (MCS) from the Gridded Satellite (GridSat)-B1 infrared (IR) brightness temperature ( $T_B$ ) data set at the same time as Figures 6a–6c. The GridSat data set are available at a 3-hr temporal resolution and  $0.07^\circ \times 0.07^\circ$  horizontal resolution (Knapp et al., 2011). An MCS is defined as a cloud of 20~200 km, a lifetime larger than 3-hr, and  $T_B$  less than 245 K (Machado et al., 1998). At 0000 UTC 19 July, the WPSH was approximately located to the north of  $26^\circ\text{N}$  and to the west of  $128^\circ\text{E}$  (red contour in Figure 6a). The MCSs were scattered around the Tai-hang Mountains and Fu-niu Mountain with weak intensities (Figure 6d). At 0000 UTC 20 July, the WPSH continually extended northwestward covering the Korean Peninsula, which was more northwestward than the climatology (yellow contour in Figure 6b). The Typhoon In-Fa, situated over the Philippine Sea to the south of the WPSH, intensified and moved northwestward (Figure 6b). Owing to the intense pressure gradient between the WPSH and In-Fa, the strong easterly/southeasterly flows can be observed, transporting abundant water vapor into Henan Province. Meanwhile, a smaller and weaker Typhoon Cempaka coexisted in the south China Sea, contributing to the northward moisture transport to Henan Province. However, its influence was confirmed to be minor compared to Typhoon In-Fa (Rao et al., 2022). Due to the blocking of low-level easterly and southerly inflows by the Tai-hang Mountains, Song-shan Mountain, and Fu-niu Mountain to the west of Henan province (Figure 6d), as well as the occurrence of MCSs in the vicinity (Figure 6e), the IMT convergence region was evident in central Henan (Figure 6b), consistent with the heavy rainfall distribution (Figure 5b). In particular, the extreme hourly rainfall at Zhengzhou station was affected by the mesoscale and even smaller-scale cloud merging during 0800–0900 UTC 20 July (not shown). After 24-hr, the MCSs were shifted southeastward, and their influence on HnHRE was weakened (Figure 6f). Influenced by the northwestward-moving WPSH, the IMT convergence center was displaced to northeastern Henan, in good agreement with the extreme precipitation distribution (Figure 5c).

## 4. Numerical Results

### 4.1. Verification of the CTL

To verify the numerical simulation, the comparison of the simulation with the observation is conducted in this section. The observed track and intensity of In-Fa is obtained from the Japan Meteorological Agency (JMA). As shown in Figure 1a, the westward track is captured well by the model (gray track in Figure 1a), but the simulated track has a northward deviation to the west of  $129^\circ\text{E}$ . Figure 1b compares the intensity of In-Fa between the JMA best track data and CTL, in terms of the minimum sea-level pressure (MSLP). Overall, CTL simulates reasonably the evolution of In-Fa intensity, except that the simulated intensity is more potent than the observed. Figure 7a displays the synoptic pattern in CTL at 0000 UTC 20 July. Although the WPSH intensity is slightly stronger than the observation, the southern and western flanks of the simulated WPSH are approximately located at  $30^\circ\text{N}$  and  $122^\circ\text{E}$ , covering the Korean Peninsula and Japan, in good agreement with the FNL data (cf., Figures 6b and 7a).

To avoid spin-up, the period from 0600 UTC 19 July to 1200 UTC 21 July is selected for study time. The spatial distribution of 54-hr accumulated rainfall in CTL (Figure 8b) is similar to the observed rainfall obtained from the China Meteorological Agency (CMA, Figure 8a), except that the simulated heavy rainfall covers a smaller area compared with the observed. The  $33.5^\circ\text{N} - 36^\circ\text{N}, 112^\circ\text{E} - 115^\circ\text{E}$  region is selected as the target region of the observation and simulations (Figure 8), which is used to compare the target-region-averaged hourly rainfall in Figure 9a. The observed two peak rainfall episodes occur during 0300–0400 and 1700–1800 UTC 20 July (black solid in Figure 9a), with the corresponding simulated peaks leading and lagging by 2- and 4-hr (gray solid in Figure 9a), respectively. The overall temporal evolution of observed precipitation is well replicated in CTL, except the latter is smaller in magnitude than the former almost during the study period. The above comparisons suggest that CTL is able to capture reasonably not only the major features of the WPSH and In-Fa, but also the overall evolution of HnHRE, providing the credibility for the following analysis.

### 4.2. Precipitation of the Sensitivity Experiments

The previous subsection displays that CTL can reproduce well the observation. In this section, the differences in the circulation systems and precipitation will be illustrated between the four sensitivity experiments and CTL.

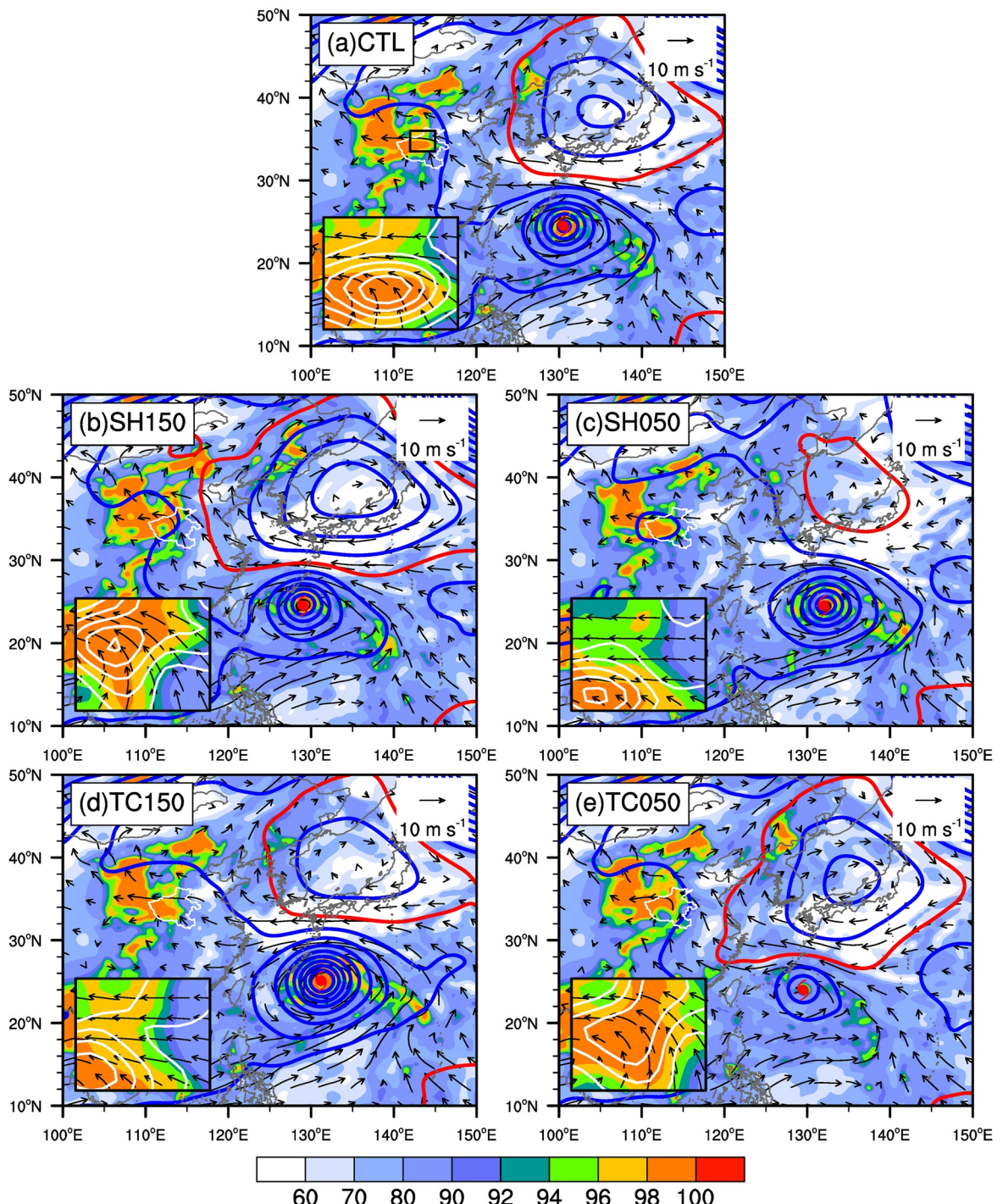


**Figure 7.** The spatial distributions of 850-hPa RH (shaded, units: %) and horizontal wind (vectors, units:  $m s^{-1}$ ), 500-hPa geopotential height (blue contours starting from 5,720 gpm with a spacing of 20 gpm with the 5,880-gpm contour in red, units: gpm) at 0000 UTC 20 July in (a) CTL, (b) SH150, (c) SH050, (d) TC150, and (e) TC050. The white line represents the boundary of Henan Province. The 850-hPa RH, wind, and  $\omega$  (white contours decreasing from  $-0.2 Pa s^{-1}$  with a spacing of  $0.2 Pa s^{-1}$ ) in the target region [black box in (a),  $33.5^{\circ}N - 36^{\circ}N, 112^{\circ}E - 115^{\circ}E$ ] are displayed in the bottom-left subgraphs of (a–e).

Figure 1a depicts the simulated Typhoon In-Fa tracks in the four sensitivity experiments. All the tracks generally move westward, although their speeds and locations are somewhat different. In SH150 (SH050), the WPSH is strengthened (weakened) by 50% and expands (shrinks) in Figure 7b (Figure 7c), while the intensity of In-Fa changes little (Figure 1b). The In-Fa track is shifted more westward and northwestward in SH150 and SH050

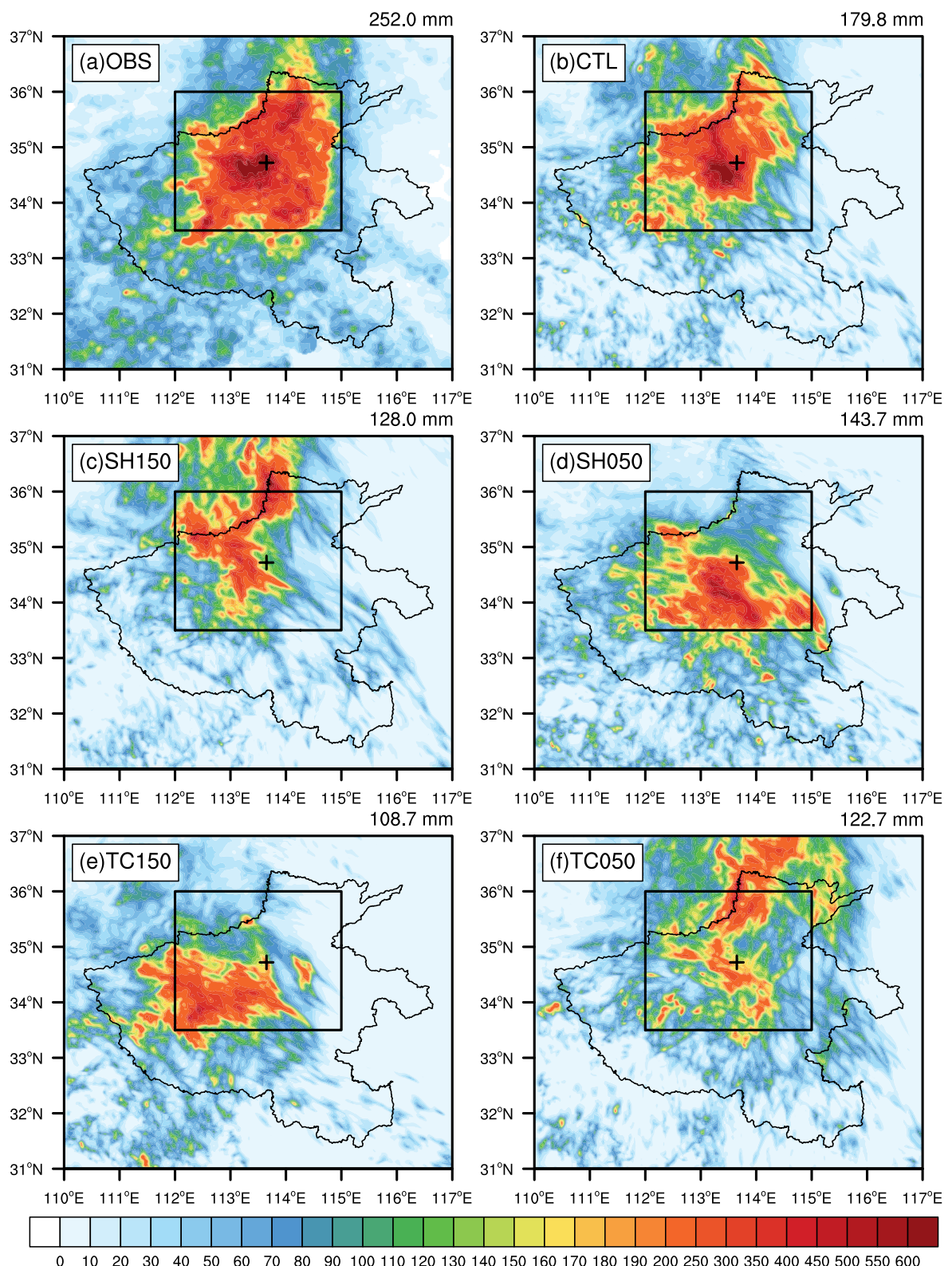


**Figure 8.** The spatial distributions of 54-hr accumulated rainfall (shaded, units: mm) in the (a) observation, (b) CTL, (c) SH150, (d) SH050, (e) TC150, (f) TC050 from 0600 UTC 19 July to 1200 UTC 21 July. The black box represents the target region ( $33.5^{\circ}\text{N}$  –  $36^{\circ}\text{N}$ ,  $112^{\circ}\text{E}$  –  $115^{\circ}\text{E}$ ). The amount of the target-region-averaged 54-hr accumulated rainfall is shown at the upper right of (a)–(f). The black line represents the boundary of Henan Province and the plus sign represents Zhengzhou station.

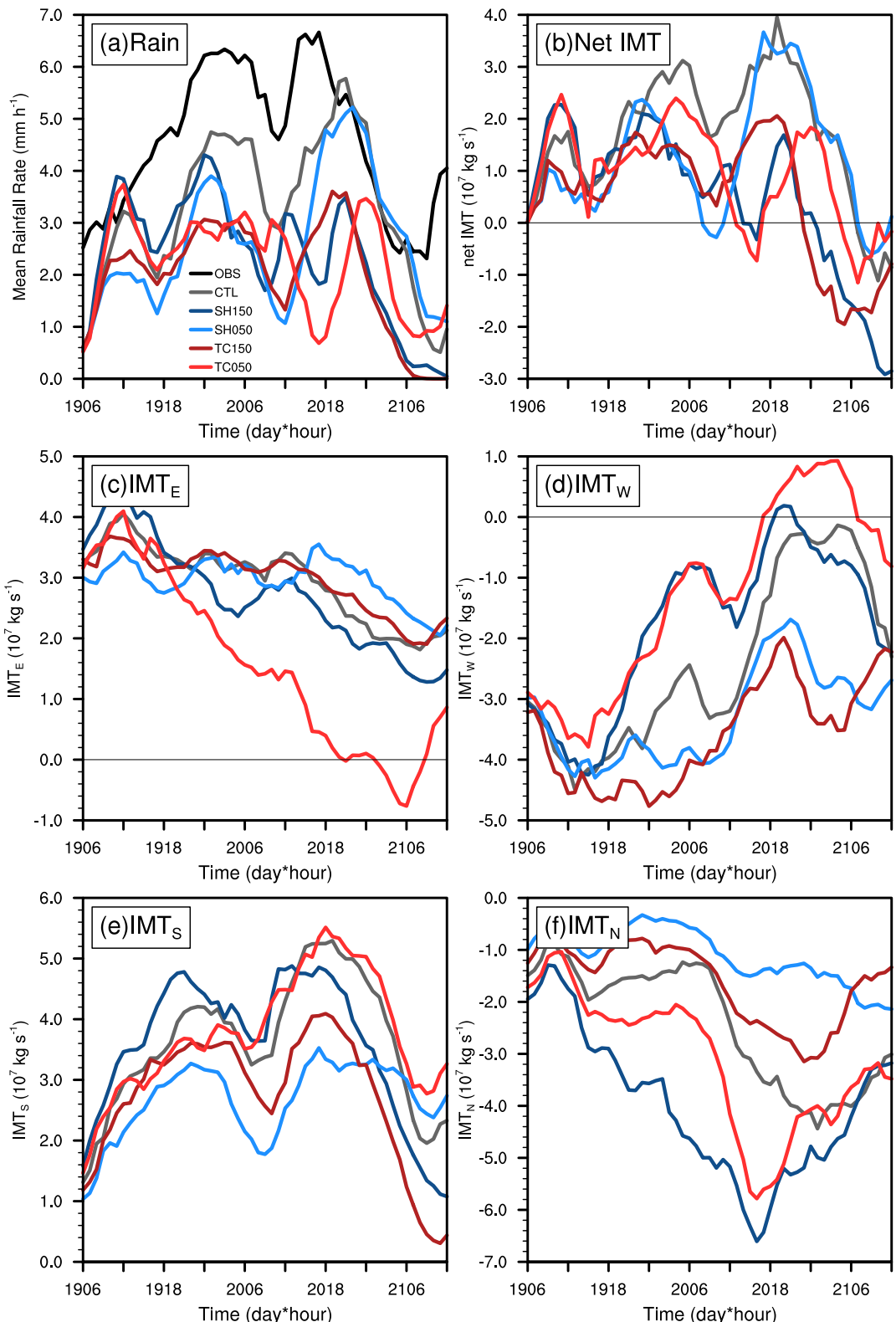


**Figure 9.** Temporal evolution of the target-region-averaged (a) hourly rainfall (units:  $\text{mm h}^{-1}$ ), (b) net IMT, (c)  $\text{IMT}_E$ , (d)  $\text{IMT}_W$ , (e)  $\text{IMT}_S$ , and (f)  $\text{IMT}_N$  (units:  $10^7 \text{ kg s}^{-1}$ ) in the observation (black solid), CTL (gray solid), SH150 (dark blue solid), SH050 (light blue solid), TC150 (dark red solid), and TC050 (light red solid) from 0600 UTC 19 July to 1200 UTC 21 July. The positive (negative)  $\text{IMT}_i$  represents moisture imports into (exports from) the target region across the  $i$  ( $i = E, W, S, N$ ) side.

than in CTL, which are similar to the NW\_60 km experiment in Xu, Duan, Li, and Wang (2022). They have demonstrated that there are small discrepancies between the NW\_60 km and control experiments. The WPSH distributions in TC150 and TC050 are similar to that in CTL (Figures 7d and 7e), except that the western and southern flanks of WPSH expand slightly in TC050 (Figure 7e). Overall, the modification of one system doesn't substantially change the other system, and thus it is feasible to distinguish the relative influence of individual systems on the HnHRE.

The precipitation differences between the four sensitivity experiments and CTL are shown in Figures 8b–8f and Figure 9a. In SH150 (SH050), the heavy rainfall is concentrated in the north (south) of the target region (Figures 8c and 8d), while the accumulated precipitation is mostly distributed in the southwest (northeast) of it in TC150 (TC050; Figures 8e and 8f). Moreover, the target-region-averaged 54-hr rainfall accumulations in TC150 and TC050 are reduced by 39.5% and 31.8%, respectively, more than 28.8% in SH150 and 20.1% in SH050, indicating that the modulation of the circulation associated with Typhoon In-Fa plays a more critical role in the rainfall amplification than the WPSH. The temporal evolutions of the hourly rainfall in the four sensitivity experiments generally keep pace with CTL (Figure 9a). One intriguing question arises as to why the original torrential rainfalls in the four sensitivity experiments target regions are significantly diminished in magnitude and less organized in distribution, irrespective of whether the WPSH or Typhoon In-Fa circulations is strengthened or weakened. To answer this question, the moisture transport, MAG  $\omega$  and the distributions of dynamic and thermodynamic factors will be analyzed in the following subsections.

#### 4.3. Moisture Transport Analysis

Some previous studies have suggested that the strong upward motion and abundant moisture are necessary ingredients for the development of rainstorms (X. Li & Du, 2021). It is evident that the evolution of the net IMT is quite consistent with the hourly rainfall in all experiments (cf., Figures 9a and 9b). In this subsection, the *IMT* across the four sides in the target region will be calculated to quantify the moisture contribution.

Due to the WPSH and In-Fa circulation adjustments, the major moisture transport channel and amount would be changed. The subgraphs of Figure 7 depict the spatial distributions of 850-hPa RH, wind and  $\omega$  in the target region at 0000 UTC 20 July. In SH150 (SH050), under the influence of the more expansive and stronger (contracted and weaker) WPSH, the southerly wind through the north (south) side of the target region (subgraphs of Figures 7b and 7c) is stronger (weaker) than that in CTL, resulting in a 64.1% (26.2%) increase (decrease) in the exported IMT<sub>N</sub> (imported IMT<sub>S</sub>) averaged from 0600 UTC 19 July to 1200 UTC 21 July. In TC150 (TC050), the stronger (weaker) easterly wind leads to a 48.7% increase (46.5% decrease) in the exported IMT<sub>W</sub> (imported IMT<sub>E</sub>) than that in CTL averaged over the study time. Compared with CTL, the high RH and strong ascending motion regions are shifted more northward, southward, westward, and northeastward in respective simulation (Figures 7b–7e), consistent with the extreme precipitation regions. The above results display that when the WPSH (In-Fa) is expansive and strong, the northward (eastward) moisture transport is increased, otherwise, it weakens. In other words, the WPSH and In-Fa majorly control the meridional and zonal moisture transports, respectively. Moreover, note that the vertical motion in each sensitivity experiment is smaller in magnitude than the counterpart in CTL, responsible for the rainfall weakening.

Figures 9c–9f show the temporal evolutions of the four-side IMT<sub>i</sub> ( $i = E, W, S, N$ ) in each simulation. Most of the IMT is imported into the target region across the east and south sides and exported from the west and north sides. The imported IMT<sub>E</sub> (IMT<sub>S</sub>) and exported IMT<sub>W</sub> (IMT<sub>N</sub>) generally decrease (increase) with time, mainly related to the westward-shifting WPSH, accompanied by the directional change of moisture transport into the target region from east-southeast to south-southeast. During most of the study period, the imported IMT<sub>E</sub> and exported IMT<sub>W</sub> in TC050 both are the minimum in all simulations due to the weakest easterly wind (light red solid in Figures 9c and 9d). The IMT<sub>S</sub> has two obvious peak periods, one is between 2000 UTC 19 July and 0600 UTC 20 July, and the other is between 1200 and 2000 UTC July 20 (Figure 9e), which are consistent with the last two peaks of net IMT, suggesting that the IMT<sub>S</sub> plays the most important role in determining the net IMT peaks. In SH150 (SH050), the imported IMT<sub>S</sub> and exported IMT<sub>N</sub> are generally larger (smaller) than those in other simulations, consistent with the stronger (weaker) southerly winds.

As we can see from Figures 7b–7f, in addition to the rainfall amounts reduction, the geographical distributions of heavy rainfall are also shifted. To explain the shift of extreme precipitation (54-hr accumulated rainfall  $>200$  mm),

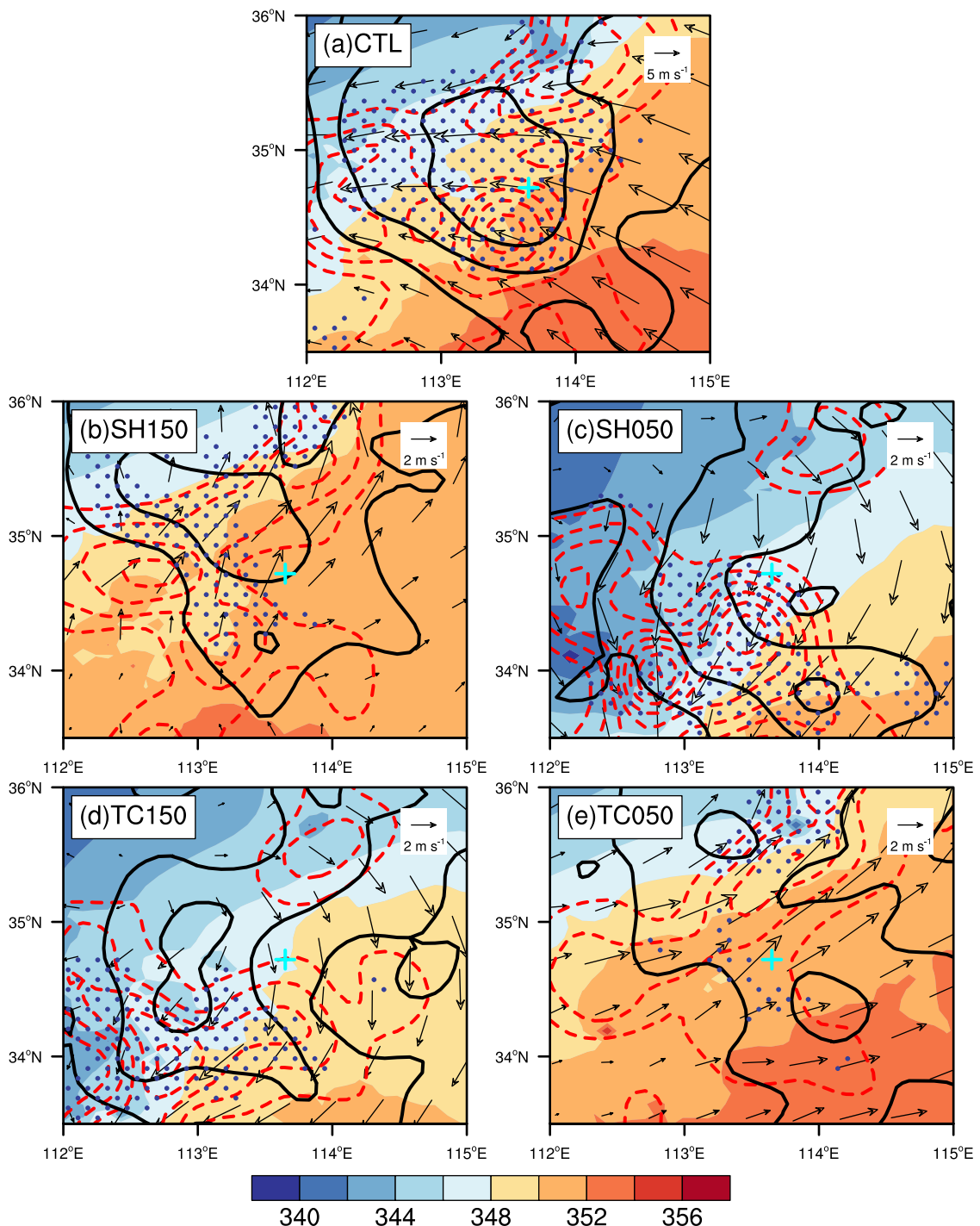


**Figure 10.** The spatial distributions of the 54-hr mean 950-hPa  $\theta_e$  (shaded, units: K), convergence (red contours decrease from  $-2 \times 10^{-5} \text{ s}^{-1}$  with a spacing of  $2 \times 10^{-5} \text{ s}^{-1}$ ), 250-hPa divergence (black contours increase from  $2 \times 10^{-5} \text{ s}^{-1}$  with a spacing of  $2 \times 10^{-5} \text{ s}^{-1}$ ), and the 54-hr accumulated rainfall (dots represent 54-hr accumulated rainfall  $> 200 \text{ mm}$ ) in (a) CTL, (b) SH150, (c) SH050, (d) TC150, and (e) TC050, together with the 54-hr mean 950-hPa wind (vectors, units:  $\text{m s}^{-1}$ ) in (a) CTL, and 950-hPa wind deviation (vectors, units:  $\text{m s}^{-1}$ ) of (b) SH150, (c) SH050, (d) TC150, and (e) TC050 from CTL. The mean field is averaged from 0600 UTC 19 July to 1200 UTC 21 July. The cyan plus sign represents Zhengzhou station.

the spatial distributions of 950-hPa  $\theta_e$ , convergence, wind deviation, and 250-hPa divergence averaged over the study time are shown in Figure 10. The 950-hPa easterly wind fields are shifted more north-northeastward (south-southwestward) in SH150 (SH050) and northeastward (southwestward) in TC050 (TC150) than in CTL. Under the influence of the wind field advection, the distinct thermal contrasts in terms of  $\theta_e$  are established more

northward (southward) in SH150 and TC050 (SH050 and TC150) compared with in CTL. The warm (cold) and moist (dry) advection from the southeast (northwest) helps facilitate heavy rainfall due to the front-like forced ascent and convective instability (Bao et al., 2015; Tsuji & Takayabu, 2019). Moreover, the 950-hPa convergence centers (red contours in Figure 10) are well concomitant with the 250-hPa divergence centers (black contours in Figure 10), in collocation with the extreme precipitation regions (dots in Figure 10). The vertical coupling of lower-level convergence and upper-level divergence is beneficial to amplify the heavy rainfall. As a result, the extreme precipitation drifts more northward, southward, southwestward, and northeastward in four sensitivity simulations than that in CTL, with attribution to the dynamical and thermal contributors.

#### 4.4. MAG $\omega$

In this subsection, the contributions of diabatic and dynamic forcings to the vertical motion are quantitatively calculated. Figure 11 presents the spatial distributions of  $\omega_{\text{MAG}}$ ,  $\omega_{\text{Dia}}$ ,  $\omega_{\text{Dyn}}$  and the convergences of  $\mathbf{Q}^*$ ,  $\mathbf{Q}_{\text{Dia}}^*$ , and  $\mathbf{Q}_{\text{Dyn}}^*$  ( $-2\nabla \cdot \mathbf{Q}^*$ ,  $-2\nabla \cdot \mathbf{Q}_{\text{Dia}}^*$ , and  $-2\nabla \cdot \mathbf{Q}_{\text{Dyn}}^*$ ) in all simulations averaged between 300 and 600 hPa from 0600 UTC 19 July to 1200 UTC 21 July.

It is obvious that the diabatic forcing is much stronger than the dynamic forcing in the mid-troposphere in all simulations. As a result, the spatial distribution of  $\omega_{\text{MAG}}$  is dominated by  $\omega_{\text{Dia}}$ , in agreement with the finding based on the quasi-geostrophic  $\omega$  equation in previous studies (Park et al., 2021; Zhao et al., 2022). As shown in Figures 11a, 11d, 11g, 11j, and 11m, the regions and relative magnitudes of high  $|\omega_{\text{MAG}}|$  and  $-2\nabla \cdot \mathbf{Q}^*$  are consistent with the heavy rainfall distributions and intensities (Figures 8b–8f), indicating that the upward motion plays an important role during the HnHRE. Although  $\omega_{\text{Dyn}}$  is much weaker than  $\omega_{\text{Dia}}$  during the HnHRE, it should be pointed out that the diabatic forcing associated with the latent heating largely rely on the triggering of dynamic forcing, especially during an initial development period (Chagnon et al., 2013; Fink et al., 2012; Grams et al., 2011; Park et al., 2021). As a result, the positive feedback between diabatic and dynamic forcings promote to augment the HnHRE.

Figure 12 presents the vertical profiles of  $\omega_{\text{MAG}}$ ,  $\omega_{\text{Dia}}$ , and  $\omega_{\text{Dyn}}$  ( $\omega_{\text{MAG}} = \omega_{\text{Dia}} + \omega_{\text{Dyn}}$ ) averaged over the target region from 0600 UTC 19 July to 1200 UTC 21 July. The derived  $\omega_{\text{MAG}}$  in CTL (gray solid in Figure 12a) overall reproduces the simulated  $\omega$  in CTL (black solid in Figure 12a), although the magnitude peak of  $\omega_{\text{MAG}}$  is situated around 450 hPa, higher than that of  $\omega$  with a peak around 600 hPa, which may be due to the boundary condition that forces  $\omega_{\text{MAG}}$  to be zero at 1,000 and 1200 hPa and the neglect of other physical processes.

Figures 12a and 12b display that diabatic heating plays a dominant role in the vertical movement across the entire troposphere during the HnHRE. The vertical averaged  $\omega_{\text{Dia}}$  accounts for 82.9%, 83.2%, 77.7%, 75.6%, 83.4% of  $\omega_{\text{MAG}}$  in CTL, SH150, SH050, TC150, and TC050, respectively. All  $\omega_{\text{MAG}}$  magnitudes in the four sensitivity experiments are smaller than that in CTL (Figure 12a), mainly associated with the weakening of latent heating released by condensing the water vapors. Note that  $\omega_{\text{MAG}}$  has a maximum magnitude at 450 hPa in all simulations, where the ample latent heating is released by the upward transport of water vapor. In contrast,  $\omega_{\text{Dyn}}$  has a peak at 350 hPa, manifesting that the critical dynamic forcing occurs in the upper level (Figures 12b and 12c). Park et al. (2021) indicated that  $\omega_{\text{Dia}}$  and  $\omega_{\text{Dyn}}$  are not independent but strongly interact with each other. The nonlinear interaction can reinforce the moisture transport, maintaining or even strengthening  $\omega_{\text{Dia}}$ .

## 5. Summary and Discussion

This study investigates the potential influences of the WPSH and In-Fa on an extreme precipitation over Henan Province in China through a series of simulations using the WRF model. The spatiotemporal evolution of the WPSH, Typhoon In-Fa (2021), and precipitation are reasonably reproduced in CTL. In SH150 and SH050 (TC150 and TC050), the strengths of  $U$ ,  $V$ ,  $\Phi$ , and  $T$  associated with the WPSH (In-Fa) are increased and decreased by 50% in the initial condition by inverting its 150% and 50% PV anomalies, respectively. A careful comparison between CTL and four sensitivity experiments is made, followed by analyzing the influences exerted by the WPSH and In-Fa on the HnHRE and the relevant physical processes. The schematic diagrams of synoptic pattern are displayed in Figure 13, with major conclusions as follows.

1. The original torrential rainfalls of the four sensitivity experiments target regions are significantly diminished in magnitude and less organized in distribution, irrespective of whether the WPSH and In-Fa circulations are strengthened or weakened relative to CTL, indicating the HnHRE occurs with the aid of the

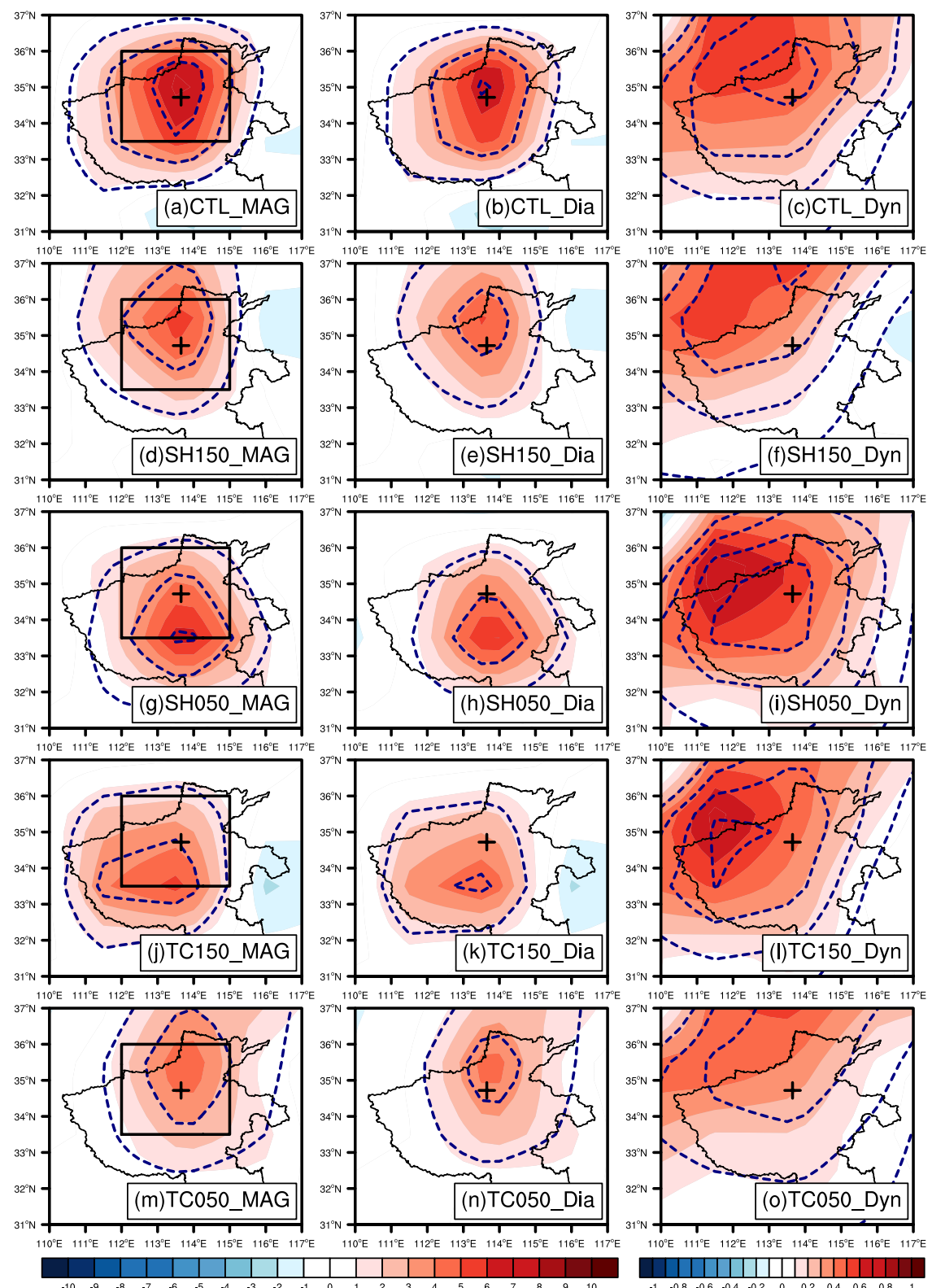


**Figure 11.** The spatial distributions of  $\omega_{\text{MAG}}$ ,  $\omega_{\text{Dia}}$  (contours decrease from  $-0.2 \text{ Pa s}^{-1}$  with a spacing of  $0.2 \text{ Pa s}^{-1}$ ),  $\omega_{\text{Dyn}}$  (contours decrease from  $-0.02 \text{ Pa s}^{-1}$  with a spacing of  $0.02 \text{ Pa s}^{-1}$ ) and the convergences of  $\mathbf{Q}^*$ ,  $\mathbf{Q}_{\text{Dia}}^*$ , and  $\mathbf{Q}_{\text{Dyn}}^*$  ( $-2\nabla \cdot \mathbf{Q}^*$ ,  $-2\nabla \cdot \mathbf{Q}_{\text{Dia}}^*$ , and  $-2\nabla \cdot \mathbf{Q}_{\text{Dyn}}^*$ , shaded, units:  $10^{-17} \text{ m kg}^{-1} \text{ s}^{-1}$ ) in (a–c) CTL (d–f) SH150, (g–i) SH050, (j–l) TC150, and (m–o) TC050 averaged between 300 and 600 hPa from 0600 UTC 19 July to 1200 UTC 21 July. Note that the color bar range of the first and second column figures is 10 times larger than that of the third column figures. The black box stands for the target region ( $33.5^\circ\text{N}$ – $36^\circ\text{N}$ ,  $112^\circ\text{E}$ – $115^\circ\text{E}$ ). The black polygon represents Henan Province and the plus sign represents Zhengzhou station.

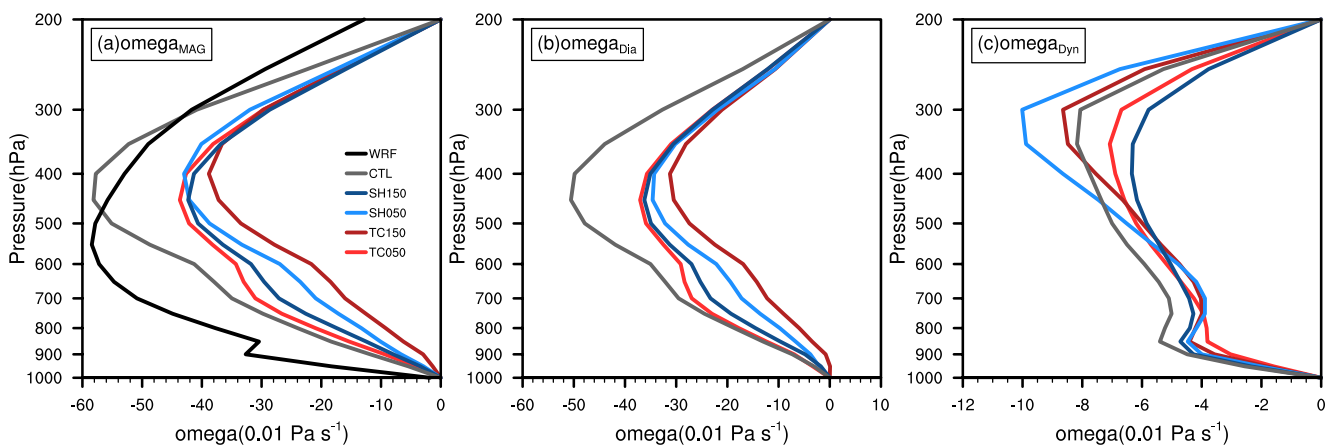


**Figure 12.** The vertical profiles of (a)  $\omega_{\text{MAG}}$ , (b)  $\omega_{\text{Dia}}$ , and (c)  $\omega_{\text{Dyn}}$  in CTL (gray solid), SH150 (dark blue solid), SH050 (light blue solid), TC150 (dark red solid), TC050 (light red solid) averaged over the target region (black box in Figures 11a, 11d, 11g, 11j, and 11m) from 0600 UTC 19 July to 1200 UTC 21 July. The black solid in (a) represents the simulated  $\omega$  from the WRF.

extremely favorable WPSH and In-Fa configuration. The analysis shows that the 54-hr accumulated rainfall in TC150 and TC050 are reduced by 39.5% and 31.8%, respectively, more than 28.8% in SH150 and 20.1% in SH050, indicating that Typhoon In-Fa plays a more critical role in the rainfall amplification than the WPSH.

2. Most of the IMT are imported into the target region across the east and south sides and exported from the west and north sides in all simulations. Due to the WPSH and In-Fa circulation adjustments, the major moisture transport channel and amount are changed. When the WPSH (In-Fa) is expansive and strong, the northward (eastward) moisture transport is increased, otherwise, it weakens (blue vectors in Figure 13). Consequently, the WPSH and In-Fa majorly control the meridional and zonal moisture transports, respectively.
3. The heavy rainfall region is largely controlled by the dynamically and thermally preferable configurations, featured by the vertical coupling of lower-level convergence and upper-level divergence and thermal contrast between high and low  $\theta_e$  air.
4. Solving the MAG  $\omega$  equation, it turns out that the vertical motion is mainly determined by the forcing related to diabatic heating during the HnHRE.  $\omega_{\text{MAG}}$  in the four sensitivity experiments is less than CTL (red upward-pointed vectors in Figure 13), due to the weakening of latent heating released by the water vapor condensation.

Moreover, to further validate our results, the two additional simulations are performed with the WPSH and Typhoon In-Fa strengthened or weakened by 50% simultaneously, denoted as SH150-TC150 and SH050-TC050. The target-region-averaged 54-hr rainfall accumulations in SH150-TC150 and SH050-TC050 are reduced by 41.8% and 19.6% compared to that in CTL (not shown), illustrating that the HnHRE occurs by means of the highly favorable WPSH and In-Fa circulations and their joint contribution. The rainfall reduction in SH150-TC150 is more than that in SH050-TC050, which is mainly related to the decreased net IMT caused by increased exported IMT and the weaker upward movement. Besides, the rainfall reduction in SH150-TC150 (SH050-TC050) is not equal to the sum of rainfall reduction in SH150 and TC150 (SH050 and TC050), indicating the effect of the WPSH and In-Fa on this heavy rainfall is nonlinear.

Our result indicated that the strong low-level easterly airflow between the WPSH and Typhoon In-Fa plays an essential role in the HnHRE, which is supported by some recent research (Deng et al., 2022; Luo et al., 2022; Y. Nie & Sun, 2022). Unique from the previous literature, the contribution of the WPSH and In-Fa to the HnHRE is reasonably and quantitatively evaluated in this study, which pointed out that the HnHRE occurred with the aid of the highly favorable configuration of WPSH and In-Fa circulations and their cooperation. In addition to these mid- and low-level synoptic systems, the upper-level systems (e.g., upper-level jet and upper-tropospheric trough) may also impact the HnHRE, which merits further study.

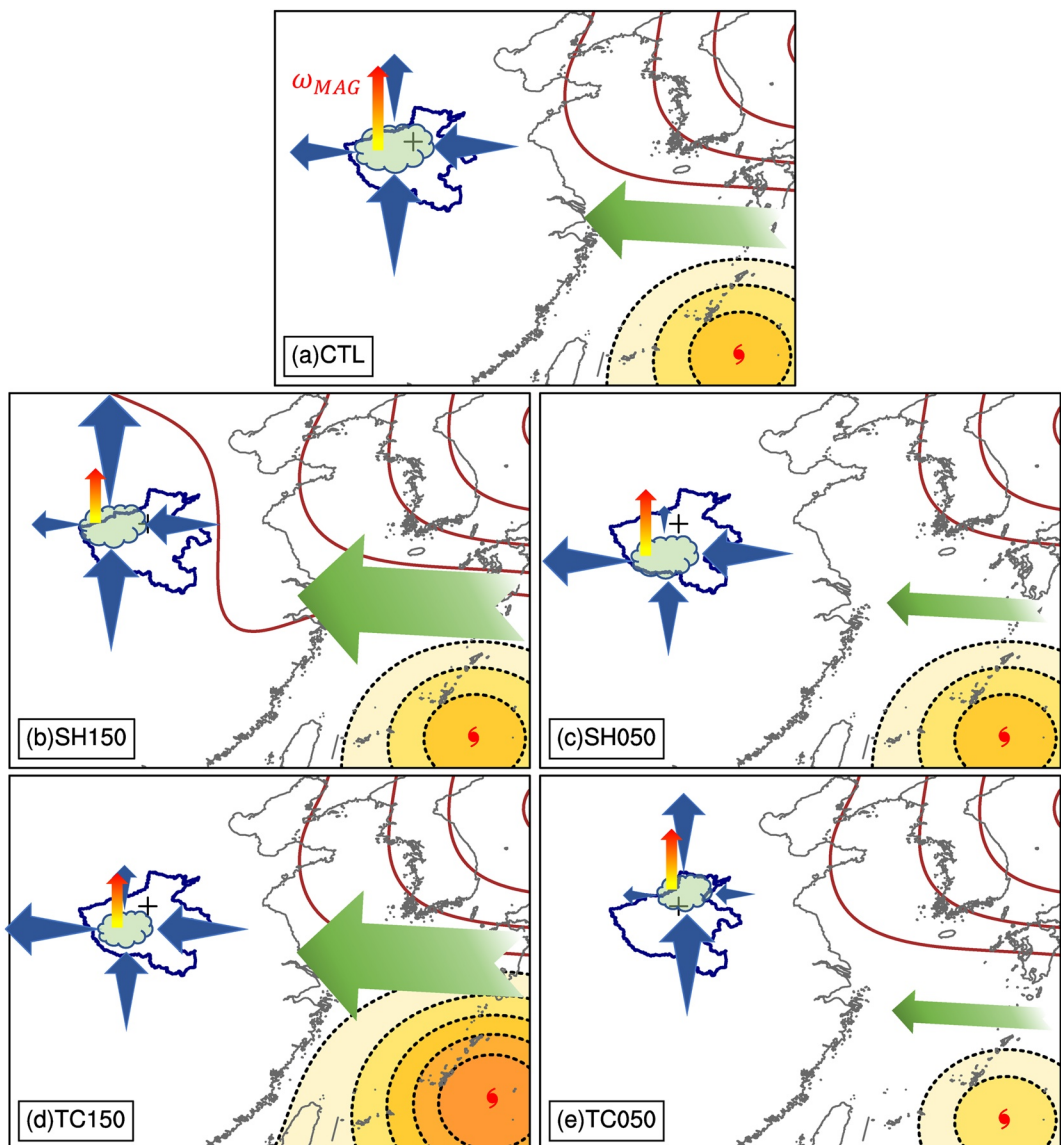


**Figure 13.** Schematic illustration of the synoptic-scale pattern in (a) CTL, (b) SH150, (c) SH050, (d) TC150, and (e) TC050. The moisture transport between the WPSH and In-Fa is denoted by green vector. The integrated moisture transport (IMT) through four sides of the target region are denoted by blue vectors.  $\omega_{MAG}$  is expressed by red upward-pointed vector. Green cloud represents rainfall region. The sizes of all signs reflect their relative contribution. The navy line represents the boundary of Henan Province and the plus sign represents Zhengzhou station.

### Data Availability Statement

The WRF-ARW model version 3.6.1 is used in this study (Skamarock et al., 2008). The FNL reanalysis data are used for the initial and boundary conditions of the model (NOAA/NCEP, 1999). The JMA best-track data is used for access to the observed track and intensity of In-Fa (JMA, 1875). The observed precipitation is from CMA precipitation data (Rao & Chen, 2022). The GridSat-B1 IR data set (Knapp, 2014) is used in this study to find MCS. The calculations and figures are made with the NCAR Command Language (NCL) version 6.6.2 (NCAR, 2019).

## Acknowledgments

This study is supported by the Strategic Priority Research Program of the Chinese Academy of Sciences (Grant XDA17010105), National Natural Science Foundation of China (Grants 42175073, 41975071), and Feng-Yun Application Pioneering Project from China Meteorological Administration (Grant FY-APP-2022.0109).

## References

- Bao, X., Davidson, N. E., Yu, H., Hankinson, M. C. N., Sun, Z., Rikus, L. J., et al. (2015). Diagnostics for an extreme rain event near Shanghai during the landfall of Typhoon Fitow (2013). *Monthly Weather Review*, 143(9), 3377–3405. <https://doi.org/10.1175/MWR-D-14-00241.1>
- Bogner, P. B., Barnes, G. M., & Franklin, J. L. (2000). Conditional instability and shear for six Hurricanes over the Atlantic Ocean. *Weather and Forecasting*, 15(2), 192–207. [https://doi.org/10.1175/1520-0434\(2000\)015<192:CIASFS>2.0.CO;2](https://doi.org/10.1175/1520-0434(2000)015<192:CIASFS>2.0.CO;2)
- Cao, J., & Gao, S. (2007). Extended interpretations in Q vector analyses and applications in a torrential rain event. *Geophysical Research Letters*, 34(15), L15804. <https://doi.org/10.1029/2007GL030781>
- Chagnon, J. M., Gray, S. L., & Methven, J. (2013). Diabatic processes modifying potential vorticity in a North Atlantic cyclone. *Quarterly Journal of the Royal Meteorological Society*, 139(674), 1270–1282. <https://doi.org/10.1002/qj.2037>
- Chen, T., Yen, M., Tsay, J., Tan Thanh, N. T., & Alpert, J. (2012). Synoptic development of the Hanoi heavy rainfall event of 30–31 October 2008: Multiple-scale processes. *Monthly Weather Review*, 140(4), 1219–1240. <https://doi.org/10.1175/MWR-D-11-00111.1>
- Davies-Jones, R. (1991). The frontogenetical forcing of secondary circulations. Part I: The duality and generalization of the Q vector. *Journal of the Atmospheric Sciences*, 48(4), 497–509. [https://doi.org/10.1175/1520-0469\(1991\)048<0497:TFFOSC>2.0.CO;2](https://doi.org/10.1175/1520-0469(1991)048<0497:TFFOSC>2.0.CO;2)
- Davis, C. A. (1992). Piecewise potential vorticity inversion. *Journal of the Atmospheric Sciences*, 49(16), 1397–1411. [https://doi.org/10.1175/1520-0469\(1992\)049<1397:PPVI>2.0.CO;2](https://doi.org/10.1175/1520-0469(1992)049<1397:PPVI>2.0.CO;2)
- Davis, C. A., & Emanuel, K. A. (1991). Potential vorticity diagnostics of cyclogenesis. *Monthly Weather Review*, 119(8), 1929–1953. [https://doi.org/10.1175/1520-0493\(1991\)119<1929:PVDOC>2.0.CO;2](https://doi.org/10.1175/1520-0493(1991)119<1929:PVDOC>2.0.CO;2)
- Deng, L., Feng, J., Zhao, Y., Bao, X., Huang, W., Hu, H., & Duan, Y. (2022). The remote effect of binary Typhoon Infra and Cempaka on the “21.7” heavy rainfall in Henan Province, China. *Journal of Geophysical Research: Atmospheres*, 127(16), e2021JD036260. <https://doi.org/10.1029/2021JD036260>
- Ding, Y., & Chan, J. (2005). The East Asian summer monsoon: An overview. *Meteorology and Atmospheric Physics*, 89(1–4), 117–142. <https://doi.org/10.1007/s00703-005-0125-z>
- Dudhia, J. (1989). Numerical study of convection observed during the winter monsoon experiment using a mesoscale two-dimensional model. *Journal of the Atmospheric Sciences*, 46(20), 3077–3107. [https://doi.org/10.1175/1520-0469\(1989\)046<3077:NSCOD>2.0.CO;2](https://doi.org/10.1175/1520-0469(1989)046<3077:NSCOD>2.0.CO;2)
- Dunn, L. B. (1991). Evaluation of vertical motion: Past, present, and future. *Weather and Forecasting*, 6(1), 65–75. [https://doi.org/10.1175/1520-0434\(1991\)006<0065:EOVMPP>2.0.CO;2](https://doi.org/10.1175/1520-0434(1991)006<0065:EOVMPP>2.0.CO;2)
- Fink, A. H., Pohle, S., Pinto, J. G., & Knippertz, P. (2012). Diagnosing the influence of diabatic processes on the explosive deepening of extratropical cyclones. *Geophysical Research Letters*, 39(7), L07803. <https://doi.org/10.1029/2012GL051025>
- Fu, S., Zhang, Y., Wang, H., Tang, H., Li, W., & Sun, J. (2022). On the evolution of a long-lived mesoscale convective vortex that acted as a crucial condition for the extremely strong hourly precipitation in Zhengzhou. *Journal of Geophysical Research: Atmospheric*, 127(11), e2021JD036233. <https://doi.org/10.1029/2021JD036233>
- Grams, C. M., Wernli, H., Bottcher, M., Campa, J., Corsmeier, U., Jones, S. C., et al. (2011). The key role of diabatic processes in modifying the upper-tropospheric wave guide: A north Atlantic case-study. *Quarterly Journal of the Royal Meteorological Society*, 137(661), 2174–2193. <https://doi.org/10.1002/qj.891>
- Gu, W., Wang, L., Hu, Z., Hu, K., & Li, Y. (2018). Interannual variations of the first rainy season precipitation over South China. *Journal of Climate*, 31(2), 623–640. <https://doi.org/10.1175/JCLI-D-17-0284.1>
- Hong, S., Dudhia, J., & Chen, S. (2004). A revised approach to ice microphysical processes for the bulk parameterization of clouds and precipitation. *Monthly Weather Review*, 132(1), 103–120. [https://doi.org/10.1175/1520-0493\(2004\)132<0103:ARATIM>2.0.CO;2](https://doi.org/10.1175/1520-0493(2004)132<0103:ARATIM>2.0.CO;2)
- Hong, S., Sunny Lim, K., Kim, J., Jade Lim, J., & Dudhia, J. (2009). Sensitivity study of cloud-resolving convective simulations with WRF using two bulk microphysical parameterizations: Ice-phase microphysics versus sedimentation effects. *Journal of Applied Meteorology and Climatology*, 48(1), 61–76. <https://doi.org/10.1175/2008JAMC1960.1>
- Horinouchi, T., & Hayashi, A. (2017). Meandering subtropical jet and precipitation over summertime East Asia and the northwestern Pacific. *Journal of the Atmospheric Sciences*, 74(4), 1233–1247. <https://doi.org/10.1175/JAS-D-16-0252.1>
- Hoskins, B. J., Draghici, I., & Davies, H. C. (1978). A new look at the  $\omega$ -equation. *Quarterly Journal of the Royal Meteorological Society*, 104(439), 31–38. <https://doi.org/10.1002/qj.49710443903>
- Hoskins, B. J., McIntyre, M. E., & Robertson, A. W. (1985). On the use and significance of isentropic potential-vorticity maps. *Quarterly Journal of the Royal Meteorological Society*, 111(470), 877–946. <https://doi.org/10.1002/qj.49711147002>
- Iacono, M. J., Mlawer, E. J., Clough, S. A., & Morcrette, J. J. (2000). Impact of an improved longwave radiation model, RRTM, on the energy budget and thermodynamic properties of the NCAR Community Climate Model, CCM3. *Journal of Geophysical Research*, 105(D11), 14873–14890. <https://doi.org/10.1029/2000JD900091>
- JMA (1875). The Regional Specialized Meteorological Center (RSMC) Tokyo-Typhoon Center. [Dataset]. Japan Meteorological Agency. Retrieved from <https://www.jma.go.jp/jma/jma-eng/jma-center/rsmc-hp-pub-eg/besttrack.html>
- Jo, E., Park, C., Son, S. W., Roh, J. W., Lee, G. W., & Lee, Y. H. (2020). Classification of localized heavy rainfall events in South Korea. *Asia-Pacific Journal of Atmospheric Sciences*, 56(1), 77–88. <https://doi.org/10.1007/s13143-019-00128-7>
- Junker, N. W., Schneider, R. S., & Fauver, S. L. (1999). A study of heavy rainfall events during the Great Midwest Flood of 1993. *Weather and Forecasting*, 14(5), 701–712. [https://doi.org/10.1175/1520-0434\(1999\)014<701:ASOHRE>2.0.CO;2](https://doi.org/10.1175/1520-0434(1999)014<701:ASOHRE>2.0.CO;2)
- Kain, J. S., & Fritsch, J. M. (1990). A one-dimensional entraining/detraining plume model and its application in convective parameterization. *Journal of the Atmospheric Sciences*, 47(23), 2784–2802. [https://doi.org/10.1175/1520-0469\(1990\)047<2784:AODEPM>2.0.CO;2](https://doi.org/10.1175/1520-0469(1990)047<2784:AODEPM>2.0.CO;2)
- Kain, J. S., Weiss, S. J., Bright, D. R., Baldwin, M. E., Levitt, J. J., Carbin, G. W., et al. (2008). Some practical considerations regarding horizontal resolution in the first generation of Operational convection-Allowing NWP. *Weather and Forecasting*, 23(5), 931–952. <https://doi.org/10.1175/WAF2007106.1>
- Knapp, K. R. (2014). NOAA climate data record (CDR) of gridded satellite data from ISCCP B1 (GridSat-B1) infrared channel brightness temperature, version 2. [Dataset]. NOAA CDR Program, NOAA National Centers for Environmental Information. Retrieved from <https://www.ncdc.noaa.gov/access/metadata/landing-page/bin/iso?id=gov.noaa.ncdc:C00829>
- Knapp, K. R., Ansari, S., Bain, C. L., Bourassa, M. A., Dickinson, M. J., Funk, C., et al. (2011). Globally gridded satellite observations for climate studies. *Bulletin of the American Meteorological Society*, 92(7), 893–907. <https://doi.org/10.1175/2011BAMS3039.1>
- Li, H., Cui, X., & Zhang, D. (2017). A statistical analysis of hourly heavy rainfall events over the Beijing metropolitan region during the warm seasons of 2007–2014. *International Journal of Climatology*, 37(11), 4027–4042. <https://doi.org/10.1002/joc.4983>
- Li, X., & Du, Y. (2021). Statistical relationships between two types of heavy rainfall and low-level jets in south China. *Journal of Climate*, 34(21), 8549–8566. <https://doi.org/10.1175/JCLI-D-21-0121.1>

- Ling, J., & Zhang, C. (2012). Diabatic heating profiles in recent global reanalyses. *Journal of Climate*, 26(10), 3307–3325. <https://doi.org/10.1175/JCLI-D-12-00384.1>
- Luo, Y., Zhang, J., Yu, M., Liang, X., Xia, R., Gao, Y., et al. (2022). On the influences of urbanization on the extreme rainfall over Zhengzhou on 20 July 2021: A convection-permitting ensemble modeling study. *Advances in Atmospheric Sciences*, 40(3), 393–409. <https://doi.org/10.1007/s00376-022-2048-8>
- Machado, L. A. T., Rossow, W. B., Guedes, R. L., & Walker, A. W. (1998). Life cycle variations of mesoscale convective systems over the Americas. *Monthly Weather Review*, 126(6), 1630–1654. [https://doi.org/10.1175/1520-0493\(1998\)126<1630:LCVOMC>2.0.CO;2](https://doi.org/10.1175/1520-0493(1998)126<1630:LCVOMC>2.0.CO;2)
- Martius, O., Schwierz, C., & Davies, H. (2008). Far-upstream precursors of heavy precipitation events on the Alpine south-side. *Quarterly Journal of the Royal Meteorological Society*, 134(631), 417–428. <https://doi.org/10.1002/qj.229>
- Meng, W., & Wang, Y. (2016). A diagnostic study on heavy rainfall induced by Typhoon Utor (2013) in south China: 1. Rainfall asymmetry at landfall. *Journal of Geophysical Research: Atmospheric*, 121(21), 12781–12802. <https://doi.org/10.1002/2015JD024646>
- Monin, A. S., & Obukhov, A. M. (1954). Basic laws of turbulent mixing in the surface layer of the atmosphere. *Tr. Akad. Nauk. SSSR Geo-phys. Inst.*, 24(151), 163–187.
- NCAR. (2019). The NCAR Command Language (version 6.6.2). [Software]. UCAR/NCAR/CISL/TDD. Retrieved from <https://www.ncar.edu/edu/Download/>
- Nie, J., & Sobel, A. H. (2016). Modeling the interaction between quasigeostrophic vertical motion and convection in a single column. *Journal of the Atmospheric Sciences*, 73(3), 1101–1111. <https://doi.org/10.1175/JAS-D-15-0205.1>
- Nie, Y., & Sun, J. (2022). Moisture sources and transport for extreme precipitation over Henan in July 2021. *Geophysical Research Letters*, 49(4), e2021GL097446. <https://doi.org/10.1029/2021GL097446>
- NOAA/NCEP. (1999). NCEP FNL Operational model global tropospheric analyses, continuing from July 1999. [Dataset]. National Centers for Environmental Prediction (NCEP) Global Final (FNL) Analysis Dataset Store. Retrieved from <https://rda.ucar.edu/datasets/ds083.2/>
- Park, C., Son, S. W., & Kim, J. H. (2021). Role of baroclinic trough in triggering vertical motion during summertime heavy rainfall events in Korea. *Journal of the Atmospheric Sciences*, 78(5), 1687–1702. <https://doi.org/10.1175/JAS-D-20-0216.1>
- Rao, C., Bi, X., Chen, G., & Yu, Z. (2022). A numerical study on the impacts of the offshore Typhoons on dynamic and thermal conditions and water vapor flux of the “21.7°” extreme rainstorm event in Henan Province. *Chinese Journal of Atmospheric Sciences*, 46, 1–18. <https://doi.org/10.3878/j.issn.1006-9895.2204.21255>
- Rao, C., & Chen, G. (2022). The observed rainfall from 0000 UTC 19 July to 1200 UTC 21 July over China. [Dataset]. Zenodo. <https://doi.org/10.5281/zenodo.7450767>
- Ross, R. J., & Kurihara, Y. (1995). A numerical study on influences of Hurricane Gloria (1985) on the environment. *Monthly Weather Review*, 123(2), 332–346. [https://doi.org/10.1175/1520-0493\(1995\)123<0332:ANSOIO>2.0.CO;2](https://doi.org/10.1175/1520-0493(1995)123<0332:ANSOIO>2.0.CO;2)
- Schumacher, R. S., Galarneau, T. J., Jr., & Bosart, L. F. (2011). Distant effects of a recurring tropical cyclone on rainfall in a midlatitude convective system: A high-impact predecessor rain event. *Monthly Weather Review*, 139(2), 650–667. <https://doi.org/10.1175/2010MWR3453.1>
- Skamarock, W. C., & Klemp, J. B. (2008). A time-split nonhydrostatic atmospheric model for weather research and forecasting applications. *Journal of Computational Physics*, 227(7), 3465–3485. <https://doi.org/10.1016/j.jcp.2007.01.037>
- Skamarock, W. C., Klemp, J. B., Dudhia, J., Gill, D. O., Barker, D. M., Wang, W., & Powers, J. G. (2008). A description of the Advanced Research WRF version 3 [Software]. Advanced Research version of the Weather Research and Forecasting Model. [https://www2.mmm.ucar.edu/wrf/users/download/get\\_source.html](https://www2.mmm.ucar.edu/wrf/users/download/get_source.html)
- Tsuji, H., & Takayabu, Y. N. (2019). Precipitation enhancement via the interplay between atmospheric rivers and cutoff lows. *Monthly Weather Review*, 147(7), 2451–2466. <https://doi.org/10.1175/MWR-D-18-0358.1>
- Viúdez, Á., Tintoré, J., & Haney, R. L. (1996). About the nature of the generalized Omega equation. *Journal of the Atmospheric Sciences*, 53(5), 787–795. [https://doi.org/10.1175/1520-0469\(1996\)053<0787:ATNOTG>2.0.CO;2](https://doi.org/10.1175/1520-0469(1996)053<0787:ATNOTG>2.0.CO;2)
- Wang, H., Sun, J., Fu, S., & Zhang, Y. (2021). Typical circulation patterns and associated mechanisms for persistent heavy rainfall events over Yangtze-Huaihe River Valley during 1981–2020. *Advances in Atmospheric Sciences*, 38(12), 2167–2182. <https://doi.org/10.1007/s00376-021-1194-8>
- Wang, X., & Zhang, D. (2003). Potential vorticity diagnosis of a simulated hurricane. Part I: Formulation and quasi-balanced flow. *Journal of the Atmospheric Sciences*, 60(13), 1593–1607. <https://doi.org/10.1175/2999.1>
- Wang, Y., Wang, Y., & Fudeyasu, H. (2009). The role of typhoon Songda (2004) in producing distantly located heavy rainfall in Japan. *Monthly Weather Review*, 137(11), 3699–3716. <https://doi.org/10.1175/2009MWR2933.1>
- Wu, C., Chen, S., Yang, C., Lin, P., & Aberson, S. D. (2012). Potential vorticity diagnosis of the factors affecting the track of Typhoon Sinlaku (2008) and the impact from dropwindsonde data during T-PARC. *Monthly Weather Review*, 140(8), 2670–2688. <https://doi.org/10.1175/MWR-D-11-00229.1>
- Wu, C., & Emanuel, K. A. (1995a). Potential vorticity diagnostics of hurricane movement. Part I: A case study of Hurricane Bob (1991). *Monthly Weather Review*, 123(1), 69–92. [https://doi.org/10.1175/1520-0493\(1995\)123<0069:PVDOHM>2.0.CO;2](https://doi.org/10.1175/1520-0493(1995)123<0069:PVDOHM>2.0.CO;2)
- Wu, C., & Emanuel, K. A. (1995b). Potential vorticity diagnostics of hurricane movement. Part II: Tropical Storm Ana (1991) and Hurricane Andrew (1992). *Monthly Weather Review*, 123(1), 93–109. [https://doi.org/10.1175/1520-0493\(1995\)123<0093:PVDOHM>2.0.CO;2](https://doi.org/10.1175/1520-0493(1995)123<0093:PVDOHM>2.0.CO;2)
- Wu, C., Huang, T., Huang, W., & Chou, K. (2003). A new look at the binary interaction: Potential vorticity diagnosis of the unusual southward movement of tropical Storm Bopha (2000) and its interaction with Supertyphoon Saomai (2000). *Monthly Weather Review*, 131(7), 1289–1300. [https://doi.org/10.1175/1520-0493\(2003\)131<1289:ANLATB>2.0.CO;2](https://doi.org/10.1175/1520-0493(2003)131<1289:ANLATB>2.0.CO;2)
- Xia, R., Luo, Y., Zhang, D., Li, M., Bao, X., & Sun, J. (2021). On the diurnal cycle of heavy rainfall over the Sichuan Basin during 10–18 August 2020. *Advances in Atmospheric Sciences*, 38(12), 2183–2200. <https://doi.org/10.1007/s00376-021-1118-7>
- Xu, H., Duan, Y., Li, Y., & Wang, H. (2022b). Indirect effects of binary typhoons on an extreme rainfall event in Henan Province, China from 19 to 21 July 2021: 2. Numerical study. *Journal of Geophysical Research: Atmospheres*, 127(15). <https://doi.org/10.1029/2021JD036083>
- Xu, H., Duan, Y., & Xu, X. (2022). Indirect effects of binary typhoons on an extreme rainfall event in Henan province, China from 19 to 21 July 2021: 1. Ensemble-Based analysis. *Journal of Geophysical Research: Atmospheric*, 127(10), e2021JD036265. <https://doi.org/10.1029/2021JD036265>
- Xu, Q. (1992). Ageostrophic pseudovorticity and geostrophic C-vector forcing-A new look at Q vector in three dimensions. *Journal of the Atmospheric Sciences*, 49(12), 981–990. [https://doi.org/10.1175/1520-0469\(1992\)049<0981:APAGCV>2.0.CO;2](https://doi.org/10.1175/1520-0469(1992)049<0981:APAGCV>2.0.CO;2)
- Yan, Z., Ge, X., Wang, Z., Wu, C., & Peng, M. (2021). Understanding the impacts of upper-tropospheric cold low on Typhoon Jongdari (2018) using piecewise potential vorticity inversion. *Monthly Weather Review*, 149(5), 1499–1515. <https://doi.org/10.1175/MWR-D-20-0271.1>
- Yanai, M., Esbensen, S., & Chu, J. (1973). Determination of bulk properties of tropical cloud clusters from large-scale heat and moisture budgets. *Journal of the Atmospheric Sciences*, 30(4), 6112–6627. [https://doi.org/10.1175/1520-0469\(1973\)030<0611:dobpot>2.0.co;2](https://doi.org/10.1175/1520-0469(1973)030<0611:dobpot>2.0.co;2)

- Yao, X., & Yu, Y. (2000). Non-geostrophic wet Q-vector analysis and its application to typhoon torrential rain. *Acta Meteorologica Sinica*, 58(4), 436–446. <https://doi.org/10.11676/qxb2000.046>
- Yao, X., Yu, Y., & Shou, S. (2004). Diagnostic analyses and application of the moist ageostrophic vector Q. *Advances in Atmospheric Sciences*, 21(1), 96–102. <https://doi.org/10.1007/BF02915683>
- Yue, C., Gao, S., Liu, L., & Li, X. (2015). A diagnostic study of the asymmetric distribution of rainfall during the landfall of typhoon Haitang (2005). *Advances in Atmospheric Sciences*, 32(10), 1419–1430. <https://doi.org/10.1007/s00376-015-4246-0>
- Yue, C., Shou, S., Lin, K., & Yao, X. (2003). Diagnosis of the heavy rain near a Meiyu front using the wet Q vector partitioning method. *Advances in Atmospheric Sciences*, 20(1), 37–44. <https://doi.org/10.1007/BF03342048>
- Zhang, D., & Kieu, C. Q. (2006). Potential vorticity diagnosis of a simulated hurricane. Part II: Quasi-balanced contributions to forced secondary circulations. *Journal of the Atmospheric Sciences*, 63(11), 2898–2914. <https://doi.org/10.1175/JAS3790.1>
- Zhang, S., Chen, Y., Luo, Y., Liu, B., Ren, G., Zhou, T., et al. (2022). Revealing the circulation pattern most conducive to precipitation extremes in Henan Province of North China. *Geophysical Research Letters*, 49(7), e2022GL098034. <https://doi.org/10.1029/2022GL098034>
- Zhang, X. (1999). An expression of the wet Q vector and application. *Meteorological Monthly*, 24(8), 3–7. <https://doi.org/10.7519/j.issn.1000-0526.1998.8.001>
- Zhang, Y., Xue, M., Zhu, K., & Zhou, B. (2019). What is the main cause of diurnal variation and nocturnal peak of summer precipitation in Sichuan Basin, China? The key role of boundary layer low-level jet inertial oscillations. *Journal of Geophysical Research: Atmospheric*, 124(5), 2643–2664. <https://doi.org/10.1029/2018JD029834>
- Zhao, Y., Chen, D., Li, J., Chen, D., Chang, Y., Li, J., & Rui, Q. (2020). Enhancement of the summer extreme precipitation over North China by interactions between moisture convergence and topographic settings. *Climate Dynamics*, 54(5–6), 2713–2730. <https://doi.org/10.1007/s00382-020-05139-z>
- Zhao, Y., Deng, L., Li, Z., & Wang, Y. (2022). Quantitative attribution of vertical motion responsible for summer heavy rainfall over North China. *Journal of Geophysical Research: Atmospheric*, 127(2), e2021JD035765. <https://doi.org/10.1029/2021JD035765>